



Mitochondrial and redox modifications in early stages of Huntington's disease

Carla Lopes^{a,b,1}, I. Luísa Ferreira^{a,b,1}, Carina Maranga^a, Margarida Beatriz^a, Sandra I. Mota^{a,b}, José Sereno^c, João Castelhanho^c, Antero Abrunhosa^c, Francisco Oliveira^c, Maura De Rosa^a, Michael Hayden^d, Mário N. Laço^{e,f}, Cristina Januário^e, Miguel Castelo Branco^{c,e}, A. Cristina Rego^{a,e,*}

^a CNC-Center for Neuroscience and Cell Biology, University of Coimbra, Coimbra, Portugal

^b IIIUC-Institute for Interdisciplinary Research, University of Coimbra, Coimbra, Portugal

^c ICNAS-Institute of Nuclear Science Applied to Health, University of Coimbra, Azinhaga de Santa Comba, Coimbra, Portugal

^d Center for Molecular Medicine and Therapeutics, Child and Family Research Institute, Department of Medical Genetics, University of British Columbia, Vancouver, Canada

^e FMUC-Faculty of Medicine, University of Coimbra, Coimbra, Portugal

^f Medical Genetics Unit, Pediatric Hospital of Coimbra, Coimbra University Hospital (CHUC), Coimbra, Portugal

ARTICLE INFO

Keywords:

⁶⁴Cu]-ATSM PET
Human skin fibroblasts
YAC128 mice
Reactive oxygen species
Mitochondrial bioenergetics

ABSTRACT

Deficits in mitochondrial function and redox deregulation have been attributed to Huntington's disease (HD), a genetic neurodegenerative disorder largely affecting the striatum. However, whether these changes occur in early stages of the disease and can be detected *in vivo* is still unclear. In the present study, we analysed changes in mitochondrial function and production of reactive oxygen species (ROS) at early stages and with disease progression. Studies were performed *in vivo* in human brain by PET using [⁶⁴Cu]-ATSM and *ex vivo* in human skin fibroblasts of premanifest and prodromal (Pre-M) and manifest HD carriers. *In vivo* brain [⁶⁴Cu]-ATSM PET in YAC128 transgenic mouse and striatal and cortical isolated mitochondria were assessed at presymptomatic (3 month-old, mo) and symptomatic (6–12 mo) stages. Pre-M HD carriers exhibited enhanced whole-brain (with exception of caudate) [⁶⁴Cu]-ATSM labelling, correlating with CAG repeat number. Fibroblasts from Pre-M showed enhanced basal and maximal respiration, proton leak and increased hydrogen peroxide (H₂O₂) levels, later progressing in manifest HD. Mitochondria from fibroblasts of Pre-M HD carriers also showed reduced circularity, while higher number of mitochondrial DNA copies correlated with maximal respiratory capacity. *In vivo* animal PET analysis showed increased accumulation of [⁶⁴Cu]-ATSM in YAC128 mouse striatum. YAC128 mouse (at 3 months) striatal isolated mitochondria exhibited a rise in basal and maximal mitochondrial respiration and in ATP production, and increased complex II and III activities. YAC128 mouse striatal mitochondria also showed enhanced mitochondrial H₂O₂ levels and circularity, revealed by brain ultrastructure analysis, and defects in Ca²⁺ handling, supporting increased striatal susceptibility. Data demonstrate both human and mouse mitochondrial overactivity and altered morphology at early HD stages, facilitating redox unbalance, the latter progressing with manifest disease.

1. Introduction

Huntington's disease is an inherited neurodegenerative disorder

* Corresponding author. CNC-Center for Neuroscience and Cell Biology, University of Coimbra, polo I, Rua Larga, 3004-504, Coimbra, Portugal.

E-mail addresses: carla.lopes@cnc.uc.pt, carlalopes09@gmail.com (C. Lopes), ildetelferreira@gmail.com (I.L. Ferreira), carinamaranga@hotmail.com (C. Maranga), margaridabeatriz@live.com.pt (M. Beatriz), sandra.mota@cnc.uc.pt (S.I. Mota), jose6sereno@hotmail.com (J. Sereno), joacastelhanho@uc.pt (J. Castelhanho), antero@pet.uc.pt, afonsoabrunhosa@gmail.com (A. Abrunhosa), francisco.oliveira@fundacaochampalimaud.pt (F. Oliveira), mauder@hotmail.it (M. De Rosa), mrh@cmmt.ubc.ca (M. Hayden), noro.laco@gmail.com, noro.laco@chuc.min-saude.pt (M.N. Laço), cristinajanuario@gmail.com (C. Januário), mbranco@fmed.uc.pt (M. Castelo Branco), arego@cnc.uc.pt, arego@fmed.uc.pt (A.C. Rego).

¹ These authors contributed equally to this work.

characterized by psychiatric, motor and cognitive symptoms, initially involving the striatum and later, other regions of the brain. Huntington's

disease platelet mitochondria) following a stress stimulus [18,19]. Evidences of redox deregulation were also found by us in *STHdh*^{Q111/Q111}

Abbreviations

BSA	Bovine serum albumin	MCU	Mitochondrial calcium uniporter
CAG	Cytosine-Adenine-Guanine	mHTT	Mutant huntingtin
EGTA	Ethylene glycol tetra-acetic acid	MIM	Mitochondrial inner membrane
ETC	Electron transport chain	mmp	Mitochondrial transmembrane potential
FCCP	Carbonyl cyanide <i>p</i> -trifluoromethoxyphenylhydrazine	NaF	Sodium fluoride
FDR	False discovery rate	NEM	<i>N</i> -ethylmaleimide
GPx	Glutathione peroxidase	OCR	Oxygen consumption rate
GRed	Glutathione reductase	ROS	Reactive oxygen species
GSH	Glutathione, reduced form	SDS	Sodium dodecyl sulphate
GSSG	Glutathione, oxidized form	SDS-PAGE	SDS polyacrylamide gel electrophoresis
HD	Huntington's disease	SOD	Superoxide dismutase
H ₂ O ₂	Hydrogen peroxide	STN	Subthalamic nucleus
HTT	Huntingtin	SUV	Standardized uptake values
		YAC	Yeast artificial chromosome

disease is linked to a dynamic mutation (an expansion in CAG repeats) located in the exon 1 of the *HTT* gene which encodes for the huntingtin (HTT) protein [1]. Expression of mutant HTT (mHTT) has been associated with mitochondrial dysfunction, including reduced mitochondrial transmembrane potential, bioenergetic abnormalities, defects in Ca²⁺ handling, alterations in organelle morphology and neurite movement, and increased production of reactive oxygen species (ROS) [2–4] largely attributed to the symptomatic stages of Huntington's disease.

Evidence of mitochondrial bioenergetic dysfunction emerged from studies in post-mortem Huntington's disease striata demonstrating defects in activities of respiratory complexes (Cx) II, III and IV and aconitase [5–7]. Huntington's disease genetic models also showed mitochondrial defects, namely reduced levels and assembly of Cx II subunits, as observed in R6/1 and Htt171-82Q transgenic mice [8]. These studies supported that mitochondrial dysfunction could contribute to the hypometabolism and progressive atrophy of the caudate in Huntington's disease. No differences were observed in respiratory activity in YAC128 mouse brain synaptic and non-synaptic mitochondria and striatal neurons [9,10], or in isolated brain mitochondria and striatal neurons from R6/2 mice [11]. Conversely, we recently showed reduced respiratory profile and decreased mitochondrial membrane potential in YAC128 mouse cortico- and striatal neurons, and unexpected increased complexes activity in isolated striatal mitochondria from younger YAC128 mouse, at 3 mo [12]. In addition, we found reduced activity of complex I and citrate synthase in mitochondrial platelets from pre-manifest Huntington's disease carriers [13]. Results in skin fibroblasts from Huntington's disease patients also demonstrated a reduction in ATP levels, suggesting a deficit of mitochondrial oxidative metabolism [14,15]. A correlation between the age of onset and bioenergetic profile was reported in fibroblast cell lines, as patients with earlier disease onset displayed more severe mitochondrial defects, independent of CAG repeat number [14]. These data implicate imbalanced mitochondrial activity in Huntington's disease human peripheral cells.

Mitochondrial dysfunction and altered mitochondrial calcium accumulation are also interconnected. Previously, we observed increased Ca²⁺ loading capacity in brain mitochondria isolated from R6/2 and YAC128 mice [16], and reduced Ca²⁺ handling in YAC128 mouse striatal neurons following elevated cytosolic Ca²⁺ due to selective activation of *N*-methyl-D-aspartate receptors [17]. A close relationship between mitochondrial deregulation and excessive ROS levels, namely superoxide anion and hydrogen peroxide, was also previously demonstrated in Huntington's disease human cybrids (retaining Huntington's

striatal cells [20,21]. Other studies in Huntington's disease human skin fibroblasts and lymphoblasts showed increased ROS levels and upregulation of antioxidant enzymes (e.g. superoxide dismutase 2, glutathione reductase, catalase) [15,22,23]. We have also shown improvement in mitochondrial function and restoration to normal in affected mice when treated with a S1R agonist, pridopidine [12].

Despite several findings indicating deregulated mitochondrial function in Huntington's disease brain and peripheral cells, data is not totally consistent while *in vivo* mitochondrial related oxidative stress namely in living Huntington's disease patients requires further elucidation. The PET radioisotope [⁶⁴Cu]-ATSM ((⁶⁴Cu)-labeled diacetyl-bis(*N*-(4)-methylthiosemicarbazone)) has been applied to visualize regional oxidative stress in patients with mitochondrial dysfunction-associated diseases [24–26]. [⁶⁴Cu]-ATSM accumulation occurs in electron rich environments, caused by mitochondrial impairment, as demonstrated in cells that are in overreduced states due to impaired mitochondrial electron transport chain (ETC) [27].

Therefore, to further elucidate the occurrence of mitochondrial dysfunction in Huntington's disease, in the present study we investigated redox changes linked to mitochondrial deregulation both in pre-manifest/prodromal *versus* manifest Huntington's disease patients and in YAC128 transgenic mouse model (at pre-/early-symptomatic to symptomatic stages) and its relationship with disease severity using [⁶⁴Cu]-ATSM. Furthermore, we correlated *in vivo* brain data with analysis of mitochondrial function, production of mitochondrial hydrogen peroxide (H₂O₂) and mitochondrial morphology in human fibroblasts (peripheral cells largely used in the study of Huntington's disease cytopathogenesis) and in isolated mitochondria derived from YAC128 mouse brain striatum and cortex at different stages of the disease to assess their relevance during disease progression.

2. Materials and methods

2.1. Human study

2.1.1. Participant's characterization

Patients and controls were selected according to clinical evaluation performed at Neurology consultation of *Centro Hospitalar e Universitário de Coimbra* (CHUC). Nine subjects were selected, six were mutant *HTT* gene carriers (Huntington's disease (HD) carriers) with ages ranging from 25 to 66 years-old, including two premanifest (pre-M1 and pre-M2), one prodromal (pre-M3) and three manifest (HD1-3), as defined by an expert neurologist, based on motor, psychiatric, and cognitive

symptoms [28], and three noncarriers/controls (C, CTR). Pre-M carriers had no signs or symptoms of Huntington's disease, while prodromal carriers had some symptoms but insufficient to make a definitive diagnosis of Huntington's disease. The age at onset was based on the date of clinical diagnosis, while the age at symptom onset was estimated on the information provided by the patient and the patient's family (Table 1). This study was performed after obtaining informed consent of all participants, according to the Declaration of Helsinki, and by following the guidelines of CHUC. The study was approved by the Ethic Committee of the Faculty of Medicine of the University of Coimbra (ref. CE-137/2015).

2.1.2. PET [^{64}Cu]-ATSM PET acquisition and processing

Preparation of [^{64}Cu]-ATSM was performed as described elsewhere [29]. Cyclotron produced [^{64}Cu]CuCl₂ solution was added to a reactor containing H₂-ATSM in CH₃COONa 1 M. The mixture was purified in a Sep-Pak tC18 light. [^{64}Cu]-ATSM was obtained in a 10% ethanol saline sterile solution, with $\geq 99\%$ of radiochemical purity and specific activity > 200 GBq/ μmol . A Philips Gemini GXL PET/CT scanner (Philips Medical Systems, Best, the Netherlands) was used to perform a dynamic 3-dimensional PET [^{64}Cu]-ATSM scan of the entire brain (90 slices, 2-mm slice sampling) and a low-dose brain CT scan, for attenuation correction. Antioxidant vitamin supplements were suspended 24 h prior to the scan.

To prevent possible head movement during acquisition, patients' head was restrained with a soft elastic tape. PET scan was acquired in a group of seven subjects (two control participants and five Huntington's disease carriers, who had clinical conditions and accepted to perform the PET study) over a period of 60 min (24 frames: $4 \times 15\text{s} + 4 \times 30\text{s} + 3 \times 60\text{s} + 2 \times 120\text{s} + 5 \times 240\text{s} + 6 \times 480\text{s}$) and started immediately after the intravenous bolus injection of approximately 925 MBq of [^{64}Cu]-ATSM. PET data were reconstructed using a LOR-RAMLA algorithm, with attenuation and scatter correction. Standard uptake value (SUV) images were calculated offline (with in-house written Matlab® quantification software) for each participant. PET and MRI data were normalized to Montreal Neurological Institute (MNI) space, the same geometric transformation was used, after the PET scan had been rigidly co-registered with the correspondent anatomical MRI scan (using SPM toolbox with default parameters; standard MRI brain was used when subject's MRI were not available). An exploratory whole-brain and region-of-interest (ROI)-based analyses were performed. Data was exported for a set of distinct regions of interest including the cerebellum, basal ganglia and subregions (putamen, caudate and subthalamic nucleus) (regions known to be affected in Huntington's disease patients). The SUV image was calculated per subject using the vessels uptake values as reference. Vessels uptake were defined as the average of the max uptake values over the first 3 min of the dynamic acquisition. Individual time-activity curves for the different ROIs and the uptake sum

were determined during 10–26 min of acquisition.

2.2. In vivo animal study

2.2.1. Animal's characterization

YAC128 transgenic hemizygous (line HD53; 128 CAG repeats) and littermate non-transgenic wild-type (WT) mice (FVB/N background) males and females, with 3 (nWT = 12; nYAC = 12), 6 (nWT = 14; nYAC = 11), 9 (nWT = 16; nYAC = 16) and 12 (nWT = 5; nYAC = 12) months of age (mo) were used, divided throughout the different experiments. All animals were generated from our local colony, with breeding couples generously provided by Dr. Michael Hayden (University of British Columbia, Vancouver, Canada). All animals were genotyped by common procedures as described in "Supplemental Methods" section. YAC128 mice exhibited an age-dependent gain of body weight (Fig. S1A), as described previously [30,31]. All studies were carried out in accordance with the guidelines of the Institutional Animal Care and Use of Committee and the European Community directive (2010/63/EU) and protocols approved by the Faculty of Medicine, University of Coimbra (ORBEA_189_2018/11,042,018).

2.2.2. [^{64}Cu]-ATSM PET/MRI acquisitions

Animal PET acquisitions were performed by using the radiopharmaceutical [^{64}Cu]-ATSM in YAC128 and WT mice at 3, 6, 9 and 12 mo. In all PET scans a prototype of a high-acceptance small-animal PET based on resistive plate chambers (RPC-PET) was used [32]. A mean activity of 418 ± 85 kBq/g was injected. The PET acquisition lasted for 60 min post injection. Volumetric images were reconstructed using OSEM algorithm and cubic voxel of 0.5 mm width. Two structural volumetric MRI T2 images were acquired per mouse using a MRI scan with the objective to facilitate the registration (geometric alignment) of the functional volumetric PET images with the volumetric MRI images, and thus allowing the segmentation of the regions of interest. A fiducial marker that can be viewed both in the PET and MRI imaging was placed in the mice bed. MRI imaging was performed after PET without moving the mice from the bed. Mice were kept anesthetized by isoflurane (1–2%) with 100% O₂ with body temperature and respiration monitoring (SA Instruments SA, Stony Brook, USA). All MRI experiments were performed in a BioSpec 9.4T MRI scanner (Bruker Biospin, Ettlingen, Germany) with a volume head coil. High resolution morphological images were acquired with a 2D T2-weighted turbo RARE sequence and axial slice orientation. The sequence for fiducial marks had the following parameters: TR/TE = 8372/33 ms, FOV = 25.6×25.6 mm, acquisition matrix = 256×256 , averages = 1, rare factor = 8, echo spacing = 11 ms, 80 axial continuous slices with 0.4 mm thick and acquisition time of 4min28s. The sequence for head mouse had the following parameters: TR/TE = 4500/33 ms, FOV = 25.6×25.6 mm, acquisition matrix = 256×256 , averages = 8, rare factor = 8, echo

Table 1:

Clinical data of Huntington's disease carriers and patient's and control groups.

	Code	CAG repeat number	Sex	Calendar age, y	Disease duration, y	Age at clinical diagnosis, y	Age at symptom onset, y	Symptom at onset	Symptoms UHDR
Control	C1	23	F	25	n.a.	n.a.	n.a.	n.a.	n.a.
	C2	25	M	46	n.a.	n.a.	n.a.	n.a.	n.a.
	C3	23	M	47	n.a.	n.a.	n.a.	n.a.	n.a.
Premanifest & Prodromal/early HD	Pre-M1	46	M	25	n.a.	22	n.a.	n.a.	2
	Pre-M2	42	M	30	n.a.	29	n.a.	n.a.	n.a.
	Pre-M3	52	F	29	7	28	22	cognitive	24
Manifest HD	HD1	43	M	62	22	47	40	psychiatric	30
	HD2	42	F	66	19	54	47	psychiatric	33
	HD3	46	F	43	7	39	36	psychiatric	72

Abbreviations: F- female; M – male; n.a.- not applied; C- controls; pre-M- premanifest Huntington's disease carriers; HD- Manifest Huntington's disease patients.

spacing = 11 ms, 42 axial continuous slices with 0.4 mm thick and acquisition time of 19min12s.

2.2.3. [^{64}Cu]-ATSM uptake quantification

Based on the fiducial marker, the volumetric images obtained from the PET were manually registered by the volumetric MRI images using the 3D Slicer 4.4 software. The volumetric MRI images were manually segmented using the ITK-SNAP 2.2 software and the segmentation results applied to the registered volumetric PET images. The mean counts per mm^3 in each ROI were computed and normalized by the activity injected per gram. Only the counts between 20- and 60-min post injection were considered.

2.3. In vitro human and animal study

2.3.1. Cell culture

Fibroblasts from Huntington's disease carriers and controls were generated from a small skin sample (about 3 mm diameter) from the abdominal region via a punch biopsy, as described previously [33] (see "Supplemental Methods" for detailed description). Fibroblasts were cultured in DMEM medium (Gibco), supplemented with 15% FBS (Gibco) and 1% penicillin/streptomycin (Gibco) and maintained to a maximum of 15 passages.

2.3.2. Isolation of functional mitochondria

Mice were weighted and then sacrificed by cervical dislocation and decapitation. Brains were removed from the skull and washed once in PBS containing (in mM): 137 NaCl, 2.7 KCl, 1.8 KH_2PO_4 , 10 $\text{Na}_2\text{HPO}_4 \cdot 2\text{H}_2\text{O}$, pH 7.4, followed by striatum and cortex dissection. Striatal and cortical mitochondrial-enriched fractions were then isolated using discontinuous Percoll density gradient centrifugation as previously described [34], and detailed in "Supplemental Methods".

2.3.3. Bioenergetic assay

The fibroblasts oxidative phosphorylation and glycolytic profile were obtained by measuring the oxygen consumption rate (OCR) and extracellular acidification ratio (ECAR) on a Seahorse XF24 or XF96 apparatus. OCR was also analysed in fresh striatal and cortical mitochondria isolated from YAC128 versus WT mice in coupling and uncoupling conditions by using a Seahorse XF24 apparatus (see "Supplemental Methods" for detailed description).

2.3.4. Measurement of cellular and mitochondrial hydrogen peroxide levels

Mitochondrial or cellular H_2O_2 levels were measured in fibroblasts using mitochondria peroxy yellow 1 (MitoPY1) (Sigma) or Amplex Red reagent and horseradish peroxidase from the Amplex® Red Catalase Assay Kit (Molecular Probes), respectively. H_2O_2 production by YAC128 and WT striatal and cortical mitochondria was measured by the Amplex® Red method. Detailed in "Supplemental Methods".

2.3.5. Transmission electron microscopy

For transmission electron microscopic (TEM) ultrastructural analyses fibroblasts were pelleted by centrifugation and striatum dissected out from 3 mo WT and YAC128 mice brain and processed as detailed in "Supplemental Methods".

2.3.6. Genomic DNA extraction and mitochondrial DNA copies

Genomic DNA was isolated from fibroblasts by means of high salt/ethanol precipitation. All DNA samples were considered pure when A260/A280 ratio was comprised between 1.8–2.0.

To quantify the average mitochondrial DNA (mtDNA) copy number of the fibroblasts the Absolute Human Mitochondrial DNA Copy Number Quantification qPCR Assay Kit (ScienCell Research Laboratories) was used according to manufacturer protocol. Briefly, a mtDNA primer set recognizes and amplifies human mtDNA and another reference primer set recognizes and amplifies a 100 bp-long region on human

chromosome 17 and serves as reference for data normalization. The reference genomic DNA sample with known mtDNA copy number serves as a reference for calculating the mtDNA copy number of target samples.

2.3.7. Mitochondrial Ca^{2+} handling capacity

Mitochondrial Ca^{2+} uptake was measured fluorimetrically using the Ca^{2+} -sensitive fluorescent dye Calcium Green-5N (150 nM; excitation and emission wavelengths of 506 nm and 532 nm, respectively) that exhibits an increase in fluorescence emission intensity upon binding to Ca^{2+} as described elsewhere [35] with minor modifications [34]; thus, a decrease in the Calcium Green fluorescence indicates the capacity of mitochondria to handle Ca^{2+} . Briefly, 5 μg of YAC128 and WT striatal or cortical isolated mitochondria was added to the incubation medium containing 125 mM KCl, 0.5 mM MgCl_2 , 3 mM KH_2PO_4 , 10 mM HEPES, 10 μM EGTA, supplemented with 3 mM pyruvate, 1 mM malate, 3 mM succinate, 3 mM glutamate, 0.1 mM ADP and 1 μM oligomycin, pH 7.4. After a basal fluorescence record, six pulses of 10 μM CaCl_2 were added every 4 min. Data are presented as traces of calcium handling capacity and plotted as extramitochondrial calcium (Extra mitoCa) for the third pulse of added calcium, as described in figure legend.

2.4. Additional methods

See *Supplementary Materials* for more comprehensive description of the mentioned methods and details on genotyping, measurement of glutathione levels and glutathione peroxidase and glutathione reductase activities.

2.5. Statistical analyses

Statistical computations were performed using GraphPad Prism version 7.0, GraphPad Software, La Jolla, CA, USA, and SPSS version 21.0 (IBM SPSS Statistics for Windows, IBM Corp). Statistical analysis was performed for individual subjects and among groups (controls, Pre-M and HD/manifest patients). For patients/controls data statistical calculations an One-Way ANOVA analysis was computed followed by a two-stage linear step-up procedure of Benjamini, Krieger and Yekutieli to correct for multiple comparisons by controlling the False Discovery Rate. For fibroblasts experiments at least three independent assays were performed for each experimental condition. Statistical significance was analysed using parametric test, two-way ANOVA, followed by Bonferroni post-hoc test and non-parametric test Kruskal Wallis followed by Dunn's multiple comparison test. Correlations were done using the Spearman rank correlation coefficient (ρ). The power analysis approach to sample size determination was done using G power software on effect size (mean/standard deviation within groups) for $1-\beta = 0.8$ and $\alpha = 0.05$. The results obtained from the animal's experiments are expressed as the mean \pm SEM of the number of replicates, considering the number of animals indicated in the figure legends. Excluded outliers were defined at GraphPad Prism 8.0.2 analyses. Comparisons among multiple groups were performed by two-way ANOVA followed by Tukey's post-hoc test. Comparison between two populations, as described in figure legends was performed by nonparametric Mann Whitney U test. Significance was defined as $p \leq 0.05$.

2.6. Data availability

The data that support the findings of this study are available from the corresponding author, upon reasonable request.

3. Results

3.1. Clinical data

From the selected nine participants for this study, six were *HTT* gene mutation carriers, classified as premanifest and prodromal (Pre-M) and

manifest HD (Table 1). Pre-M carriers had no clinical motor signs or symptoms insufficient to make the diagnosis of Huntington's disease, based on standardized total motor score of Unified Huntington Disease Rating Scale (UHDRS) [36]. Huntington's disease carriers had CAG repeats ranging from 42 to 52; the prodromal patient exhibited the longest repeat expansion and an anticipated phenotypic onset, compared to age-matched Huntington's disease carriers. Manifest HD patients showed symptoms and signs of Huntington's disease. Furthermore, symptoms at onset varied from psychiatric (manifest HD patients) and cognitive (prodromal Huntington's disease carrier) symptoms.

3.2. Increased accumulation of [⁶⁴Cu]-ATSM in premanifest Huntington's disease carriers

Whole brain and regional PET [⁶⁴Cu]-ATSM retention in the SUV images was compared between groups (Huntington's disease carriers, Pre-M and HD, and controls) using statistical parametric mapping and ROI analysis. Increased accumulation of [⁶⁴Cu]-ATSM was observed in the Pre-M Huntington's disease carriers, when compared to the control group in brain mask, cerebellum and subthalamic nucleus (STN) ($p < 0.05$). The exception was the caudate as the SUV decreased with disease severity ($p = ns$), suggesting neuronal degeneration (Fig. 1A–C). Spearman correlation analyses showed that [⁶⁴Cu]-ATSM brain accumulation in whole brain and STN directly correlates with CAG repeat number ($\rho = 0.709$, $p = 0.074$; $\rho = 0.746$, $p = 0.05$, respectively) (Fig. 1D and E).

Enhanced [⁶⁴Cu]-ATSM complex entrapment and labelling was observed in the majority of brain areas in Pre-M Huntington's disease carriers, which could be related with increased intracellular

overreductive state due to excessive release of electrons derived from modified mitochondrial respiratory chain, as previously described [24, 25,27,37].

3.3. Altered mitochondrial function and redox deregulation in premanifest/prodromal Huntington's disease carriers

To test whether [⁶⁴Cu]-ATSM PET labelling could be related with modified mitochondrial function and enhanced production of ROS, potentially revealing an overreduced intracellular state, and while mitochondrial respiratory chain activity cannot be directly measured in human brains, we assessed the changes in mitochondrial function and ROS levels in human skin-derived fibroblasts obtained from the same controls and Huntington's disease mutation carriers (Pre-M and HD), detailed in Table 1.

Comparisons of oxygen consumption rates (OCR) between groups showed that basal and maximal respiration are enhanced in Pre-M versus controls, accompanied by increased H⁺ leak ($p < 0.05$), as measured indirectly based on respiration measurements (Fig. 2A–D). By contrast, manifest HD patients demonstrated a general decrease in basal (vs controls, $p < 0.01$), maximal and spare respiration and H⁺ leak (vs Pre-M, $p < 0.05$) (Fig. 2A–D). No significant differences in ATP production (Fig. 2A–D), ATP/ADP ratio or energy charge (Fig. S2) were found in Huntington's disease carriers, when compared to the control group. The observed increase in H⁺ leak in Pre-M cells (above control conditions) with no accompanying rise in ATP synthesis is suggested to be responsible for the increase in respiration.

Interestingly, we observed a strong and statistically significant inverse correlation between individual disease duration, age of symptoms

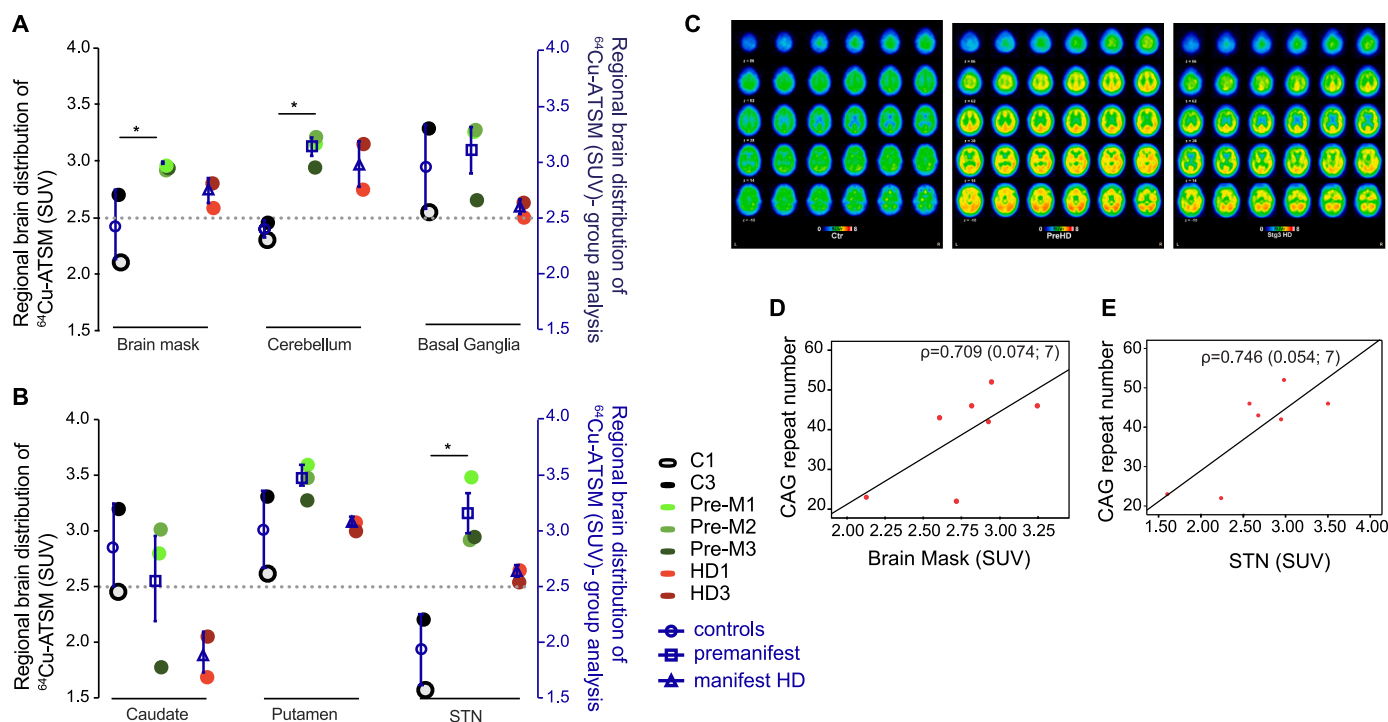


Fig. 1. [⁶⁴Cu]-ATSM brain accumulation in premanifest and manifest Huntington's disease patients and correlation with CAG repeats. [⁶⁴Cu]-ATSM brain PET imaging of Huntington's disease carriers and controls was evaluated in cerebellum and basal ganglia (A) and basal ganglia subregions: caudate, putamen and subthalamic nucleus (STN) (B) of controls (C), premanifest (Pre-M) and manifest Huntington's disease patient's (HD) brains, as described in Methods section. (C) Representative axial slices of PET imaging of the three groups analysed (left to right): controls, premanifest and manifest Huntington's disease carriers; PET color scale indicates the uptake of the [⁶⁴Cu]-ATSM normalized for cerebral blood vessels SUVs. Correlation between CAG repeat number and normalized SUV of [⁶⁴Cu]-ATSM uptake from total brain (brain mask) (D) and uptake from STN (E). Regional brain distribution of [⁶⁴Cu]-ATSM (A)(B) was calculated as the sum of three time-points SUVs between 14 and 22 min acquisition time; mean \pm SEM values of the groups are plotted on the secondary Y axis (blue). (D)(E) Correlation was performed using the Spearman correlation coefficient ρ (sig; n). SUV - standardized uptake values. Statistical analysis: One-Way ANOVA corrected for multiple comparisons by false discovery rate (FDR) using two-stage linear step-up procedure of Benjamini, Krieger and Yekutieli. * $p < 0.05$ (controls vs premanifest). (For interpretation of the references to color in this figure legend, the reader is referred to the Web version of this article.)

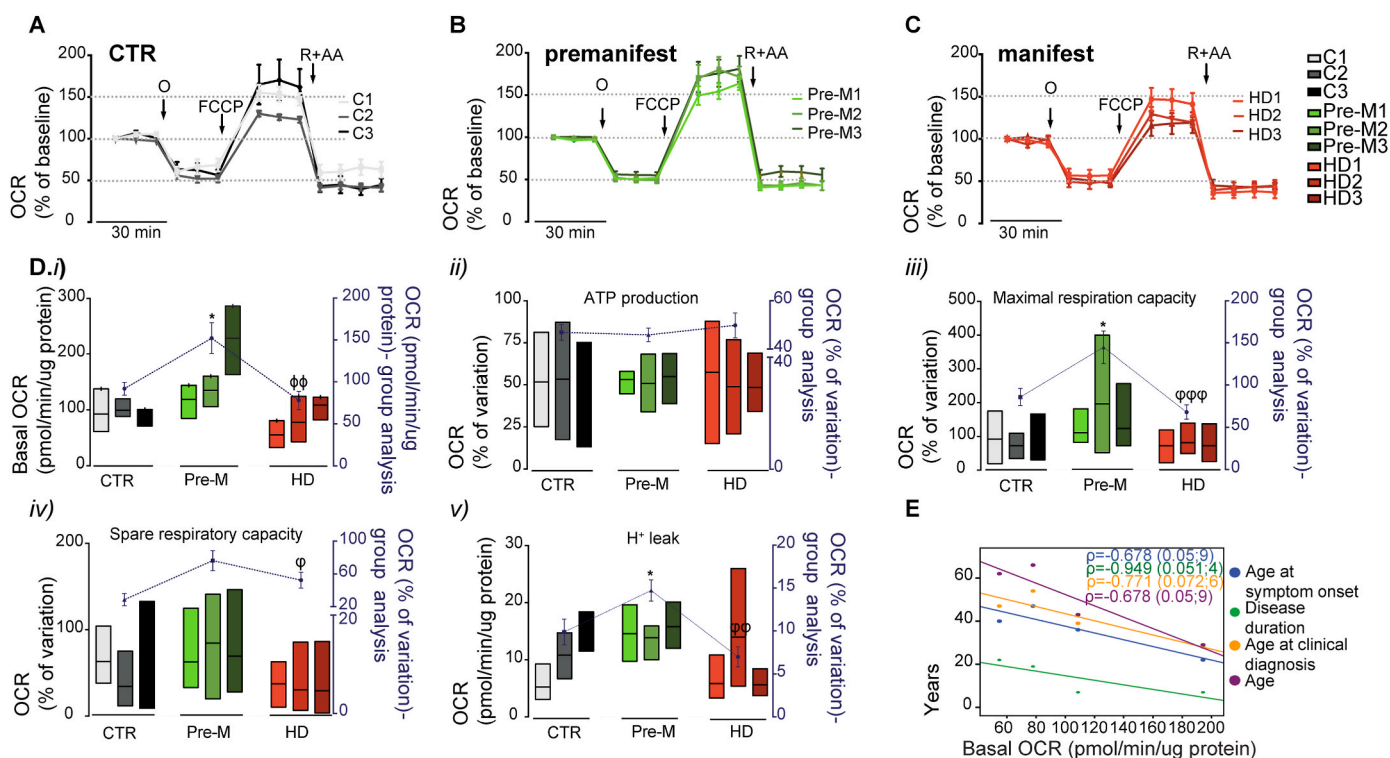


Fig. 2. Oxygen consumption rate (OCR) in skin fibroblasts from premanifest and manifest Huntington's disease carriers and controls. (A–C) OCR of cells treated with the different compounds. The mitochondrial inhibitors were sequentially injected into different ports of the Seahorse XF24 analyzer and the final concentrations of each were: 1 μ M oligomycin (O), 0.3 μ M FCCP (F), 1 μ M rotenone and 1 μ M antimycin A (R + A). (D) (i) Levels of basal OCR; (ii) Oxygen consumed for ATP generation through the complex V; (iii) Maximal respiration capacity; (iv) Spare respiratory capacity; (v) Component of OCR representing passive H⁺ leakage across the mitochondrial inner membrane were calculated as described in Methods section; individual data are presented as floating bars (min, max) with mean lines shown at least three independent experiments; group analysis represents the mean \pm SEM values (controls (C, CTR), premanifest (Pre-M) and manifest HD patients) and are plotted on the secondary Y axis (blue). (E) Correlation was performed using the Spearman correlation coefficient ρ (sig; n). Statistical analysis: One-Way ANOVA – post hoc Bonferroni's multiple comparisons test. * $p < 0.05$ (controls vs premanifest); $^{**}p < 0.01$ (controls vs HD manifest) and $^{*}p < 0.05$, $^{***}p < 0.01$, $^{****}p < 0.001$ (premanifest vs HD manifest). (For interpretation of the references to color in this figure legend, the reader is referred to the Web version of this article.)

onset and chronological age with basal OCR. Longer disease duration ($\rho = -0.949$, $p = 0.05$), more advanced age at symptom onset ($\rho = -0.678$, $p = 0.05$) and at clinical diagnosis ($\rho = -0.770$, $p = 0.07$) and older age ($\rho = -0.678$, $p = 0.05$), the later corresponding to two Huntington's disease manifest patients, was accompanied by lower absolute values of basal respiration (Fig. 2E).

We also analysed glycolytic parameters by assessing extracellular acidification rates (ECAR) in human skin fibroblasts derived from the same individuals. Data showed no major differences between groups, except for the glycolytic capacity of manifest HD patients that had lower absolute values, when compared to controls ($p < 0.05$) and to Pre-M Huntington's disease carriers ($p < 0.01$) (Fig. S3).

Because mitochondrial dysfunction is largely associated with increased of ROS production, potentially triggering an overreduced state associated with [⁶⁴Cu]-ATSM accumulation, the relative levels of mitochondrial and cellular-derived H₂O₂ were measured in human skin fibroblasts using MitoPY1 and Amplex Red, respectively (Fig. 3). We found significantly higher levels of cellular H₂O₂ in fibroblasts derived from Pre-M carriers, which were further elevated with disease progression (Fig. 3A). Interestingly, a significant rise in basal levels of mitochondrial H₂O₂ (mito-H₂O₂) was observed in more advanced stages of Huntington's disease (Fig. 3B). Following complex III inhibition with myxothiazol (3 μ M), the levels of mito-H₂O₂ increased with disease severity, being significantly higher in cells derived from manifest HD patients *versus* controls ($p < 0.05$) (Fig. 3C). Correlation analysis showed augmented cellular H₂O₂ levels in Huntington's disease carriers with longer CAG repeat number ($\rho = 0.769$, $p = 0.05$), and a lower uptake of [⁶⁴Cu]-ATSM in the caudate was associated with increased cellular H₂O₂

levels ($\rho = -0.714$, $p = 0.071$) (Fig. 3D and E).

These data indicate early increased mitochondrial respiration in Pre-M carriers that is not accompanied by ATP production, but rather promotes redox dysregulation through enhanced cellular ROS levels, which is further enhanced in cells from manifest HD.

3.4. Premanifest and prodromal Huntington's disease carriers show decreased circularity and increased mitochondrial DNA copies correlated to higher [⁶⁴Cu]-ATSM uptake

Because mitochondrial dysfunction has been linked to changes in mitochondrial morphology, we analysed the morphometric parameters of mitochondria that were individually traced from TEM images obtained in human skin fibroblasts (Fig. 4A). We measured the major mitochondrial shape factors, namely area, circularity (an index of sphericity), Feret's diameter, perimeter, form factor, and aspect ratio (Fig. 4B). Mitochondria from Pre-M Huntington's disease carriers show decreased circularity, are more elongated (higher Feret's diameter), have more complex and branched networks and larger aspect ratios (length/width ratio) when compared with the control or manifest HD patients (Fig. 4A and B; Suppl. Table 1) ($p < 0.05$). Decreased mitochondrial circularity in Pre-M fibroblasts may indicate that mitochondria are less fragmented. However, slight increased circularity was observed in fibroblasts from patients with manifest HD, when compared to the controls and Pre-M carriers. Fibroblasts from Pre-M Huntington's disease carriers showed a higher absolute number of mtDNA copies, although non-significant when compared to CTR ($371,460 \pm 59,452$ vs $216,717 \pm 43,034$), whilst manifest HD patients showed reduced

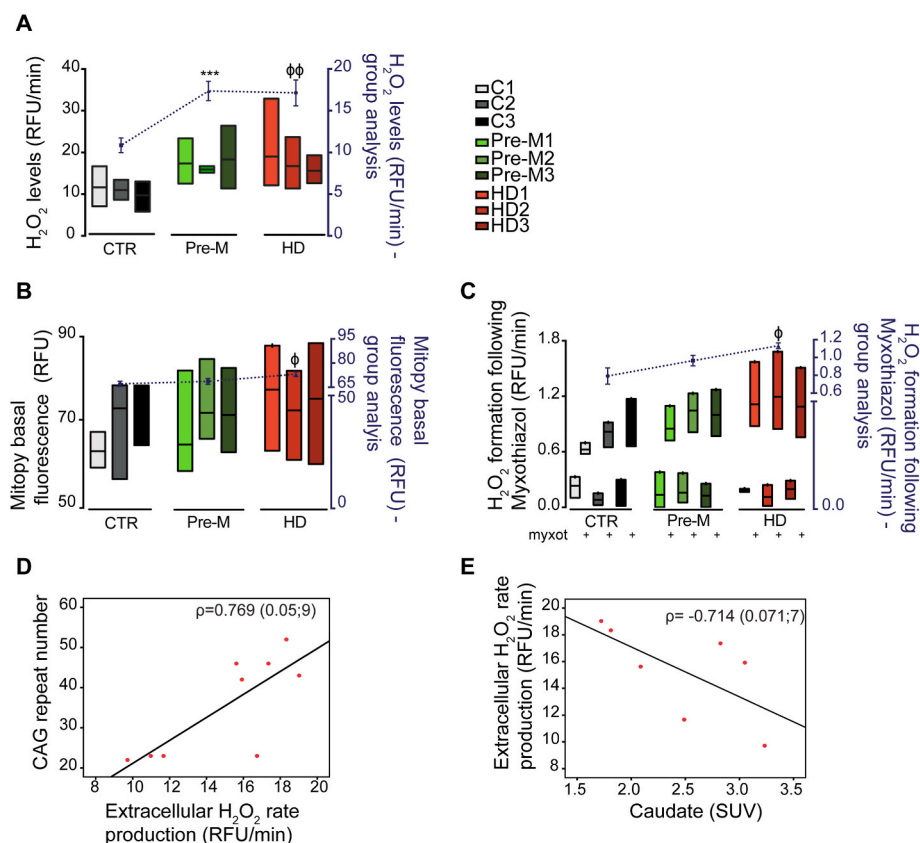


Fig. 3. Cellular and mitochondrial ROS levels in skin fibroblasts from Huntington's disease patient's and controls - correlation with CAG repeats and [⁶⁴Cu]ATSM uptake in caudate. Cellular-derived (A) and basal mitochondrial (B) H₂O₂ production were measured as described in Methods section and was plotted as bars graph. (C) Time-dependent H₂O₂ production in the mitochondria after stimulation with complex III inhibitor-myxothiazol (3 μM). Individual data are presented as floating bars (min, max) with mean lines shown at least 3 independent experiments; group analysis represents the mean ± SEM values (controls (C, CTR), pre-symptomatic (Pre-M) and manifest HD patients) and are plotted on the secondary Y axis (blue). (D)(E) Correlation was performed using the Spearman correlation coefficient ρ (sig; n). Statistical analysis: non-parametric Kruskal-Wallis test followed by Dunn's Multiple Comparison Test. *** $p < 0.001$ (controls vs premanifest); and $^{\phi}p < 0.05$, $^{\phi\phi}p < 0.01$ (controls vs HDs). (For interpretation of the references to color in this figure legend, the reader is referred to the Web version of this article.)

mtDNA copy number, when compared to cells from Pre-M ($147,490 \pm 28,476$ vs $371,460 \pm 59,452$, $p < 0.05$) (Fig. 4C). Furthermore, we observed that human skin fibroblasts with higher number of mitochondrial DNA copies have significantly greater spare ($\rho = 0.867$, $p = 0.01$) and maximal respiratory capacity ($\rho = 0.783$, $p = 0.05$). In addition, patients with longer disease duration have a lower number of mtDNA copies ($\rho = -0.949$, $p = 0.041$). Interestingly, enhanced mtDNA copy number was positively correlated with augmented [⁶⁴Cu]-ATSM uptake in whole brain ($\rho = 0.786$, $p = 0.036$), cerebellum ($\rho = 0.679$, $p = 0.094$), basal ganglia ($\rho = 0.75$, $p = 0.052$) and putamen ($\rho = 0.857$, $p = 0.014$). These data may suggest that Pre-M Huntington's disease carriers showing higher number of mtDNA copies in peripheral cells also have higher accumulation of [⁶⁴Cu]-ATSM in selected brain areas.

3.5. Enhanced [⁶⁴Cu]-ATSM brain accumulation in YAC128 mouse brain

In order to verify whether changes in [⁶⁴Cu]-ATSM brain accumulation correlate with mitochondrial changes in affected areas in Huntington's disease brain, we further analysed *in vivo* [⁶⁴Cu]-ATSM accumulation by PET and studied mitochondrial fractions isolated from the striatum and cortex of YAC128 mice along aging.

In vivo age-dependent analysis of intracellular overreductive status was also evaluated in YAC128 versus wild-type mice over the progression of the disease, at 3 (pre-symptomatic), 6 (early-symptomatic) and 9 and 12 (symptomatic) months of age (mo), through the analysis of [⁶⁴Cu]-ATSM accumulation in the striatum (Fig. 5A and B) and frontal cortex (Fig. 5A,C). Statistical analysis by two-way ANOVA revealed a significant genotype ($F(1,35) = 12.07$; $p = 0.0014$) and age-dependent ($F(3,35) = 36.67$; $p < 0.0001$) [⁶⁴Cu]-ATSM accumulation in the striatum (Fig. 5Bi). *In vivo* data obtained in the cortex also demonstrated an age-dependent effect ($F(3,38) = 12.61$; $p < 0.0001$) and a slight, but significant, genotype effect ($F(1,38) = 4.192$; $p = 0.0476$) in [⁶⁴Cu]-

ATSM accumulation (Fig. 5Ci). In addition, when [⁶⁴Cu]-ATSM accumulation in YAC128 mouse striatum or cortex were replotted in relation to the respective WT mice, a significant increase in the radioligand accumulation was observed in the striatum of 6 mo ($p < 0.05$) and a trend at 12 mo ($p = 0.0571$) (Fig. 5Bii), but not in the cortex (Fig. 5Ci).

3.6. Increased oxygen consumption rate, complexes II and III activities and oxidative status in striatal mitochondria derived from pre-symptomatic YAC128 mice

The respiratory activity in striatal and cortical isolated mitochondrial-enriched fractions derived from YAC128 and WT mouse brain striatum and cortex was analysed by determining OCR and complexes activities (Fig. 6 and S4). Notably, both wild-type HTT and mHTT were shown to associate with cortical- and striatal-enriched isolated mitochondria derived from WT and YAC128 mice, respectively (Fig. S1C).

Coupling experiments performed under Cx II feeding (in the presence of succinate) and Cx I inhibition (with rotenone) in striatal mitochondria obtained from 3 mo YAC128 mice showed increased basal and maximal respiration and ATP production, but unchanged H⁺ leak, (Fig. 6Ai), when compared to WT mice. In order to further explain these changes in OCR, we analysed the electron flow through mitochondrial respiratory chain, to evaluate Cx I-IV activities under conditions of direct mitochondrial feeding (pyruvate, to generate acetyl-CoA) plus malate (to activate the TCA cycle) in the FCCP-induced uncoupled state.

In agreement with results obtained in Fig. 6Ai, striatal mitochondria obtained from 3 mo YAC128 mice exhibited a significant increase in Cx II and III activities, but unaltered activities in Cx I and IV (Fig. 6Aii), when compared with WT mouse mitochondria. No significant changes in mitochondrial-coupled respiration parameters or Cx I-IV activities were observed in cortical mitochondria (at 3, 6, 9 and 12 mo) (Fig. 6 Bi and Bii; Fig. S4Bi and S4Bii) or striatal mitochondria obtained from older

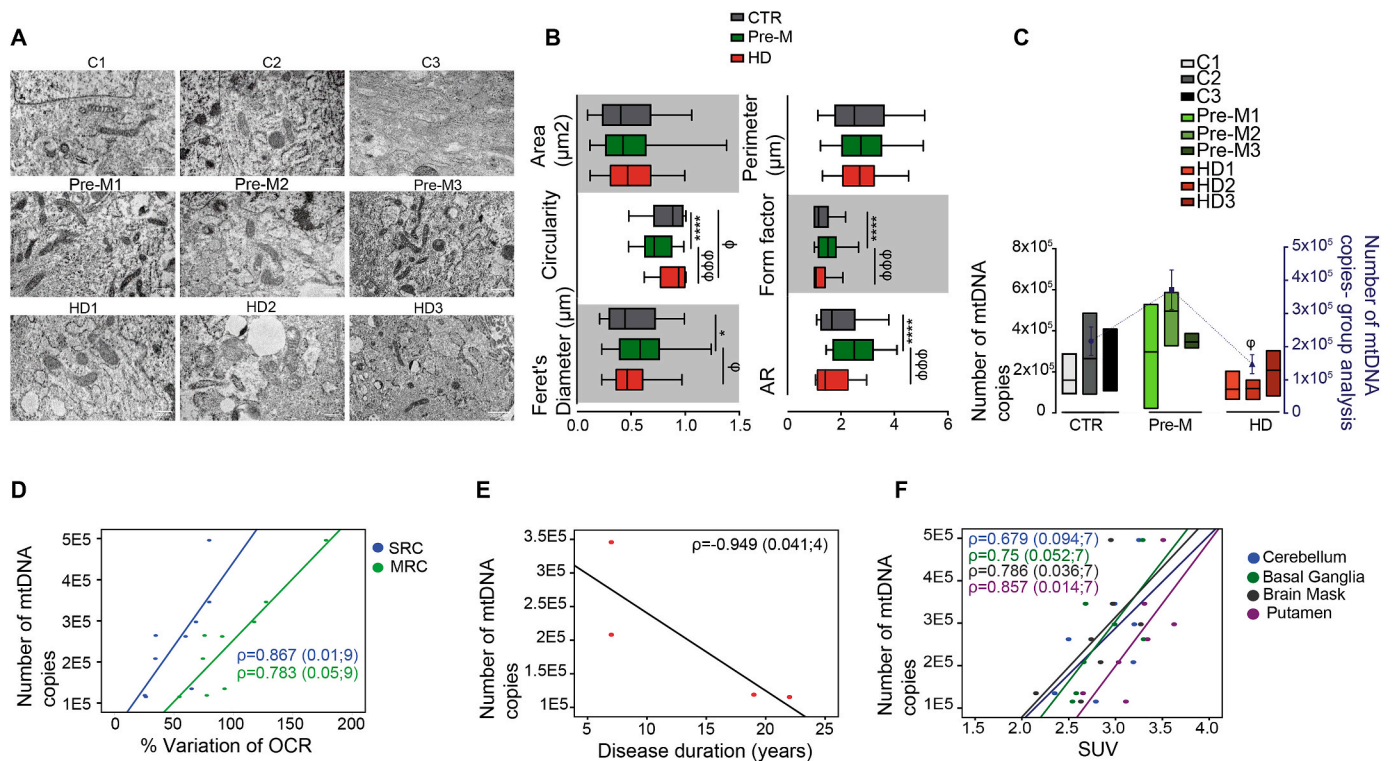


Fig. 4. Mitochondrial morphological features and DNA copy number in fibroblasts derived from premanifest and manifest Huntington's disease carriers and controls - correlation with $[^{64}\text{Cu}]$ -ATSM uptake, disease duration and OCR. (A) Transmission electron microscopy (TEM) representative images of mitochondrial ultrastructure. **(B)** Analysis of morphological parameters for mitochondria area, circularity, Feret's diameter, perimeter, form factor and aspect ratio made using ImageJ software. The results are expressed as the mean \pm SEM of mitochondria counted by images ($n = 9$ –26) from a total of $n = 29$ –122 mitochondria analysed. Bars represent the median and interquartile range [percentiles 5–95] for each parameter. Statistical analysis: ANOVA followed post-hoc Bonferroni test: **** $p < 0.0001$ (controls vs pre-symptomatic); * $p < 0.05$, (controls vs HDs) and $^{pp}p < 0.001$ (pre-M vs HDs). **(C)** Number of mitochondrial DNA copies quantified as described in Methods section. Individual data are presented as floating bars (min, max) with mean lines shown at least 3 independent experiments; group analysis represents the mean \pm SEM values (controls (C, CTR), premanifest (Pre-M) and manifest HD carriers) and are plotted on the secondary Y axis (blue). Statistical analysis: non-parametric Kruskal-Wallis test followed by Dunn's Multiple Comparison Test. * $p < 0.05$ (pre-M vs HDs). **(D-F)** Correlation was performed using the Spearman correlation coefficient ρ (sig; n). In **D** the variation of OCR refers to the % of variation of spare respiratory capacity (SRC) and maximal respiratory capacity (MRC) relatively to basal levels (100%). Scale bar: 2000 nm. (For interpretation of the references to color in this figure legend, the reader is referred to the Web version of this article.)

YAC128 mice (at 6, 9 and 12 mo) (Fig. S4Ai and S4Aii). Data suggest a striatum-specific increase in mitochondrial respiratory chain activity and Cx II and III activity in mitochondria from pre-symptomatic YAC128 mice.

As in human fibroblasts, we further analysed the levels of mitochondrial H_2O_2 produced by *ex vivo* striatal- and cortical mitochondrial-enriched fractions isolated from pre-symptomatic (3 mo) and symptomatic (6, 9 and 12 mo) YAC128 mice and age-matched WT mice (Fig. 7Ai and 7Aii). Results evidenced a small but significant increase in H_2O_2 production by striatal mitochondria from both pre- (3 mo; $p < 0.05$) and late-symptomatic (12 mo; $p < 0.01$) mice (Fig. 7Ai) and by cortical mitochondria from late symptomatic YAC128 mice, at 12 mo ($p < 0.05$) (Fig. 7Aii) without significant changes in intermediate ages (6 and 9 mo) for both brain areas.

Elevated mito- H_2O_2 levels were not accompanied by compromised antioxidant defenses in YAC128 mice at 3 and 9 mo. No significant changes were observed in mitochondrial acetyl (K68)SOD2/SOD2 or SOD2 protein levels in both striatum (Fig. S5Ai) and cortex (Fig. S5Bi), reduced (GSH) and oxidized (GSSG) glutathione total levels in striatum (Fig. S5Aii and S5Aiii, respectively) or cortex (Fig. S5Bii and S5Biii, respectively), nor glutathione peroxidase and reductase activities in both striatum (Fig. S5Aiv and S5Av, respectively) and cortex (Fig. S5Biv and S5Bv, respectively). This was seen despite significant decreased glutathione reductase protein levels in mitochondria from 3 mo YAC128 mouse striatum ($p < 0.05$) (Fig. S5Avi), but not in the cortex (Fig. S5Bvi).

Similarly, no differences in antioxidants at 12 mo in striatum or cortex were observed (data not shown).

3.7. Early Ca^{2+} deregulation and altered ultrastructure in YAC128 mouse striatal mitochondria

Because altered mitochondrial Ca^{2+} retention may serve as an indicator of mitochondrial impairment, we next evaluated Ca^{2+} handling in isolated striatal and cortical mitochondrial-enriched fractions from 3 mo YAC128 and WT mice. Mitochondrial Ca^{2+} uptake was monitored after sequential additions of $10 \mu\text{M}$ Ca^{2+} to raise intramitochondrial Ca^{2+} concentration in 3 mo striatal (Fig. 7Bi, upper panel) and cortical (Fig. 7Bi, lower panel) mitochondria.

Under these conditions, Ca^{2+} was sequentially taken up by both striatal and cortical mitochondria (Fig. 7Bi). However, the response to the 3rd pulse of Ca^{2+} produced a decrease in Ca^{2+} retention in striatal ($p < 0.05$; Fig. 7Bi, upper panel, detailed in dashed green window), but not in cortical (Fig. 7Bi, lower panel, detailed in dashed green window) YAC128 mitochondria, when compared to WT mitochondria, as evaluated by extramitochondrial Ca^{2+} (Extra-mitoCa) quantification. The following pulse of Ca^{2+} in striatal (Fig. 7Bi, upper panel), but not in cortical (Fig. 7Bi, lower panel) mitochondria exceeded the mitochondrial Ca^{2+} retention capacity, with a subsequent abrogation of Ca^{2+} uptake, as represented by upward deflection of the trace.

Our data highlight defects in Ca^{2+} handling in striatal mitochondria

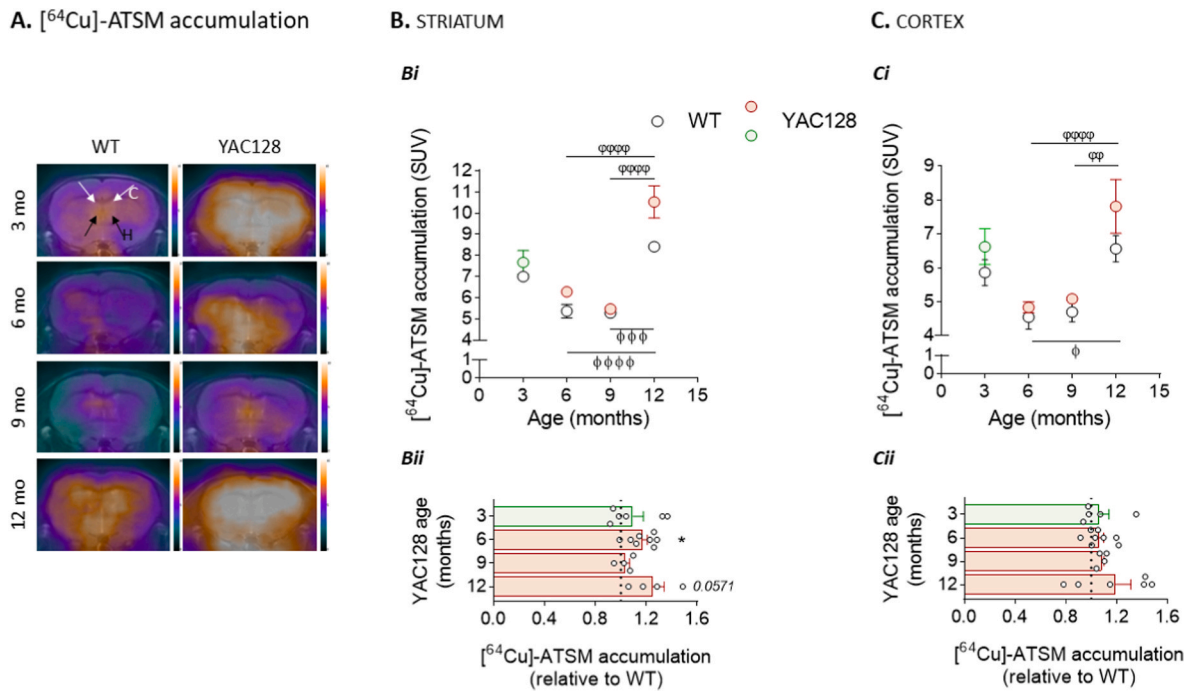


Fig. 5. Age-dependent $[^{64}\text{Cu}]$ -ATSM brain accumulation in YAC128 and WT mouse striatum and cortex. $[^{64}\text{Cu}]$ -ATSM PET and MRI overlapped axial images of brain YAC128 and WT mice where PET color scale indicates the uptake (number of counts per mm^3) of the $[^{64}\text{Cu}]$ -ATSM normalized by the injected activity, mass of the mouse and sensibility of the PET equipment. White arrows point to frontal cortex and black arrows to striatum (A). $[^{64}\text{Cu}]$ -ATSM accumulation was plotted for striatum (B) and cortex (C) at 3, 6, 9 and 12 mo YAC128 vs WT mice and in relation to WT for each age, for striatum (Bii) and cortex (Cii). Results are presented in relation to the unit (dashed line) representing WT mouse values. Data are the mean \pm SEM of acquisitions from 4 to 8 mice per group. Statistical analysis: $^{\text{p}}\text{p}<0.001$, $^{\text{pp}}\text{p}<0.001$, $^{\text{ppp}}\text{p}<0.0001$, when compared between ages in WT mitochondria and $^{\text{pp}}\text{p}<0.01$, $^{\text{pppp}}\text{p}<0.0001$ when compared between ages in YAC128 mitochondria by Two-way ANOVA followed by Sidak's multiple comparisons test. $^*\text{p} < 0.05$ when compared with 6 mo WT mitochondria by nonparametric Mann-Whitney U test. SUV - standardized uptake values. (For interpretation of the references to color in this figure legend, the reader is referred to the Web version of this article.)

derived from pre-symptomatic YAC128 mice, exhibiting lower Ca^{2+} thresholds after repeated Ca^{2+} loads. Ca^{2+} taken up by WT and YAC128 striatal-derived mitochondria was shown to be released through a FCCP-induced "releasable pool" (Fig. 7Bii) and prevented by pre-incubation with the mitochondrial Ca^{2+} uniporter (MCU) inhibitor, Ru360 (Fig. 7Bii). This indicates that Ca^{2+} retention occurred through the MCU in polarized mitochondria. Similar results were observed in cortical mitochondria (data not shown).

In order to investigate YAC128 mouse striatal mitochondrial morphology, electron micrographs obtained by TEM of 3 mo YAC128 and WT mouse striatum were assessed using quantitative measures for mitochondrial morphology (Fig. 7C). Over 154 individual mitochondria were assessed for area, perimeter, aspect ratio and circularity (Fig. 7D). YAC128 mouse striatal mitochondria showed significantly increased area and perimeter, along with decreased aspect ratio and increased circularity, when compared to WT mitochondria.

These observations suggest deregulated YAC128 mouse striatal mitochondria at presymptomatic disease stage.

4. Discussion

This work is the first to demonstrate higher accumulation of $[^{64}\text{Cu}]$ -ATSM in premanifest and prodromal (Pre-M) Huntington's disease human carriers and in an pre-symptomatic animal model in different brain regions. However, in human caudate, a region reported to be affected in the prodromal phase and showing progressive atrophy along the course of the disease due to neuronal loss [38–40], a progressive reduction in the mean SUV was observed. Our results also show that fibroblasts from Pre-M carriers and striatal mitochondria derived from pre-symptomatic YAC128 mice exhibit increased mitochondrial H_2O_2 levels, which is unrelated to decreased antioxidant levels or activity, but rather with an apparently compensatory enhanced activity of

mitochondrial respiratory chain and altered organelle morphology.

Classically, disease burden is defined based on CAG repeat length and age. In this study we show a correlation between imaging of the whole brain and particularly the STN and the number of CAG repeats. The STN is a key component of the basal ganglia and several reports, in animal models, argue that STN dysfunction and neuronal loss precede cortico-striatal abnormalities in Huntington's disease, which might contribute to motor impairment, and explain the greater accumulation of $[^{64}\text{Cu}]$ -ATSM in Pre-M individuals [42,43].

Although the copper uptake mechanism is still controversial, high levels of $[^{64}\text{Cu}]$ -ATSM retention appear to be indicative of an over-reductive state [27]. Colombi and co-authors postulated that $[^{64}\text{Cu}]$ -ATSM uptake is linked to redox potential and ROS, potentially constituting a promising marker of intracellular overreduced states for disorders with mitochondrial dysfunction [41]. Nevertheless, the effectiveness of $[^{64}\text{Cu}]$ -ATSM for hypoxia mapping has been demonstrated in several *in vitro* and *in vivo* pre-clinical models [37,41]. In the present study the overreduced microenvironment found in Pre-M Huntington's disease carriers was correlated to an overall increase in basal and maximal mitochondrial respiration in skin fibroblasts. Nevertheless, ATP synthesis remained unaffected, probably due to an increase in H^+ leak. The glycolysis parameters did not differ among the three groups, except for the glycolytic capacity that was decreased in manifest HD only, suggesting a secondary process to disease progression. In skin fibroblasts, we also found lower values of basal OCR in Huntington's disease patients correlating with earlier age of clinical diagnosis and age at onset, with longer disease duration and increased age. Additionally, a lower mitochondrial network fragmentation occurred, concomitantly with a tendency for upregulation in mtDNA copy number in peripheral cells from Pre-M Huntington's disease carriers. Importantly, the higher mtDNA copy number observed in Pre-M carriers correlates with enhanced mitochondrial respiration and increased accumulation of

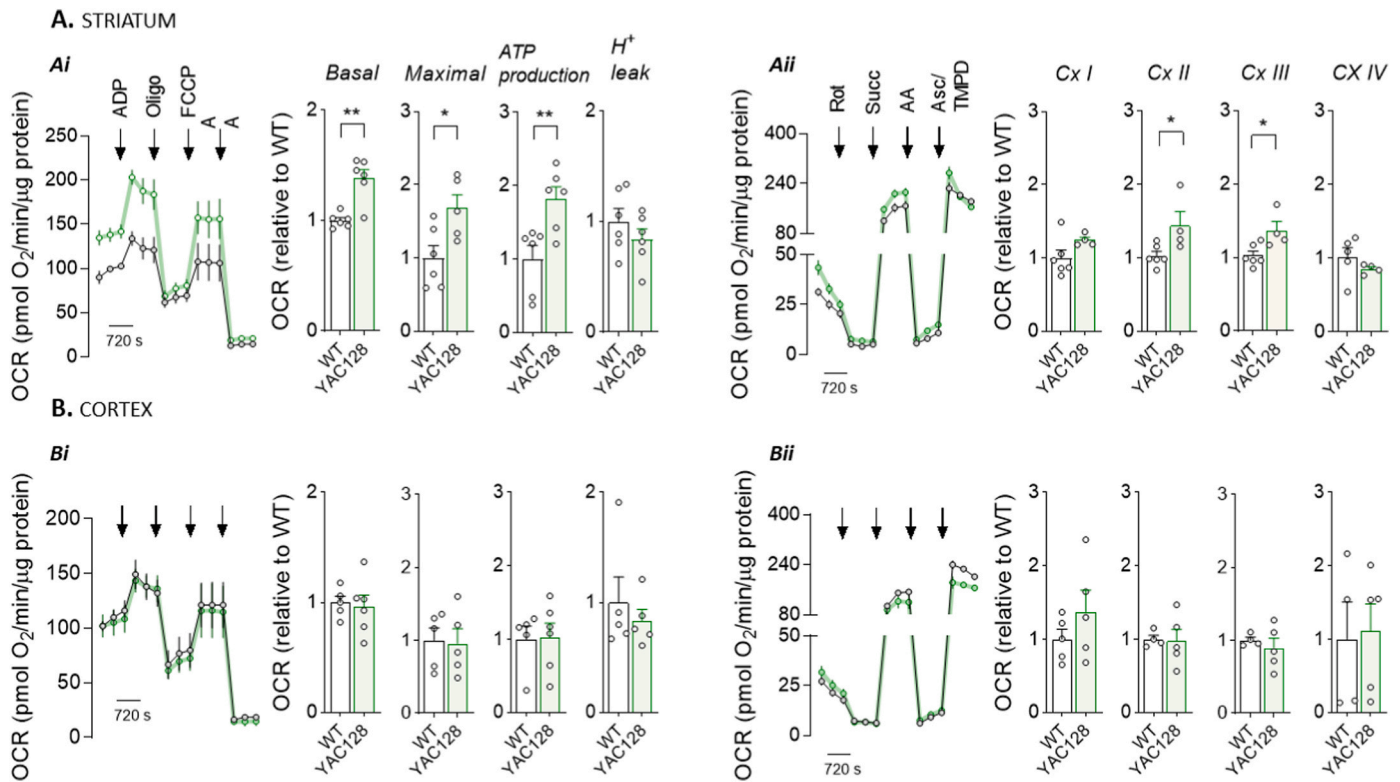


Fig. 6. Oxygen consumption rates (OCR) in 3 mo YAC128 mouse striatal and cortical mitochondria. Mitochondrial respiration was measured using the Seahorse flux analyzer in 3 mo YAC128 and WT striatal (A) and cortical (B) isolated mitochondria. Levels of respiratory coupling (Ai and Bi; for striatal and cortical mitochondria, respectively) were analysed in MAS containing 10 mM succinate plus 2 μ M rotenone under sequentially injection of mitochondrial inhibitors and substrates (final concentration: 4 mM ADP; 2.5 μ g/mL oligomycin; 4 μ M FCCP and 4 μ M antimycin A) as shown in representative traces and basal respiration and maximal respiration, ATP production and H^+ calculated as described in Methods section. The activity of mitochondrial respiratory chain complexes (Aii and Bii; for striatal and cortical mitochondria, respectively) was analysed in uncoupling conditions performed in MAS containing 4 μ M FCCP, 10 mM pyruvate and 2 mM malate. Mitochondrial inhibitors and substrates were sequentially injected (final concentration: 2 μ M rotenone, 10 mM succinate, 4 μ M antimycin A and 10 mM ascorbate/100 μ M TMPD) as shown in the representative traces and Cx I-IV activities calculated as described in Methods section. Data are the mean \pm SEM of experiments performed in independent mitochondrial preparations obtained from 3 to 7 mice from each genotype, run in duplicates or triplicates. Statistical analysis: * $p < 0.05$, ** $p < 0.01$ when compared with WT mitochondria, by nonparametric Mann-Whitney U test.

[64 Cu]-ATSM, the later most probably a reflex of altered redox status.

Strikingly, many of the hallmarks of aging itself are similar to the mechanisms involved in HD pathology, which may have accounted for by some of our findings. Most of the processes described in our study decline with aging, although in HD patients they seem to be exacerbated. The role of chronological age at onset and disease duration are actively under investigation to understand the link between aging and neurodegeneration. Notably, and as would be expected, the manifest HD group has a higher chronological age and longer disease duration associated to worse mitochondrial deficits, compared to controls or Pre-M carriers, suggesting a synergistic interplay between aging and degeneration. Indeed, brain aerobic glycolysis and mitochondrial function decrease during normal human aging [44,45]. Nevertheless, a recent study showed that, although the age of HD patients can be an important factor, disease duration seems to be more relevant since HD patients suffering for longer periods of time show more severe deficits in several indices of mitochondrial respiration, independently of their calendar age [14].

In YAC128 mice, increased [64 Cu]-ATSM retention was mostly evident in the striatum of 6 and 12 mo and less manifest in the cortex. Interestingly, striatal isolated mitochondria (but not cortical mitochondria) derived from pre-symptomatic (3 mo) YAC128 mice exhibited not only increased levels of H_2O_2 , but also enhanced activity of complexes II and III, linked to increased basal and maximal OCR and ATP production. Increased complexes activity and H_2O_2 levels were recently observed by us in isolated YAC128 mouse striatal mitochondria at 3 mo [12] and in R6/2 mouse striatal synaptic mitochondria [46]. The

increase in mitochondrial ATP generation in striatal mitochondria contrasts with human fibroblasts showing unchanged ATP levels, probably due to H^+ leakage. In addition, striatal mitochondria from pre-symptomatic YAC128 mice showed defects in Ca^{2+} handling and altered mitochondrial morphology, suggesting deregulated mitochondrial function despite the increase in mitochondrial respiratory activity, which precedes the increase in [64 Cu]-ATSM retention, at 6 mo.

Altered striatal mitochondrial function observed in this study implicates enhanced susceptibility of this brain region, consistently with previous reports showing a highly susceptibility of the striatum to impaired mitochondrial oxidative phosphorylation [47] and age-dependent striatal volumetric changes defined through longitudinal structural imaging in the YAC128 mouse model [48]. Unchanged OCR in YAC128 mouse mitochondria at 6–12 mo may be accounted for by alternative metabolic profile and/or decreased striatal energy demand, as demonstrated by enhanced levels of creatine and phosphocreatine, determined by spectroscopy (1H-MRS) [48].

Several studies have established a link between [64 Cu]-ATSM accumulation, mitochondrial dysfunction, impairment of mitochondrial respiratory chain, due to hypoxia, and related oxidative stress [26,27,49], suggesting that dysfunctional mitochondrial electron transport chain causes an overreduced state due to ROS generation, as detailed in this work. Furthermore, in a patient with MELAS (mitochondrial encephalopathy, lactic acidosis, and stroke-like episode), caused by a mitochondrial mutation, [62 Cu]-ATSM accumulation reflected changes in regional oxidative stress [26]. Increased ROS production and mitochondrial dysfunction were also described in Parkinson's disease and

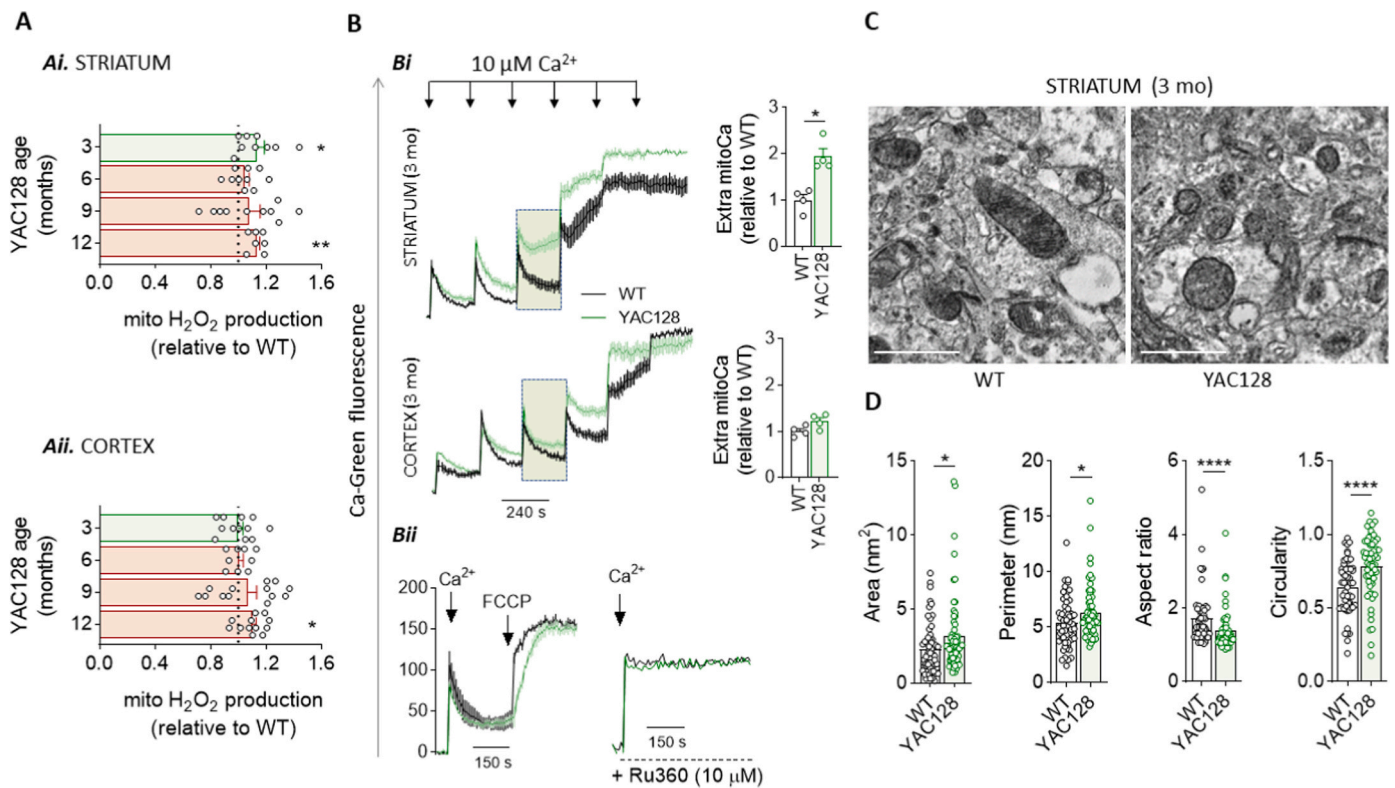


Fig. 7. Mitochondrial ROS levels, Ca^{2+} handling, and mitochondrial ultrastructure in YAC128 mouse striatal and cortical mitochondria. H_2O_2 production was measured in functional isolated mitochondria (A) derived from 3, 6, 9 and 12 mo YAC128 and WT mice striatum (Ai) and cortex (Aii) using the Amplex Red assay as described in Methods section. The capacity to handle Ca^{2+} was evaluated in striatal and cortical mitochondria obtained from 3 mo YAC128 and WT mice (B) by using Calcium Green-5N fluorescent probe. Pulses of 10 μM Ca^{2+} were applied to raise intramitochondrial Ca^{2+} concentrations until the Ca^{2+} retention capacity was reached as shown by the upward deflection of the traces (Bi). The Ca^{2+} handling capacity for striatal and cortical mitochondria at the third Ca^{2+} pulse is detailed in the dashed green window and presented as extra-mitochondrial Ca^{2+} (area under the curve) (Bi, inset). The effect of the mitochondrial uncoupler FCCP and the pharmacological inhibition of the mitochondrial calcium uniporter (MCU; Ru360) are also depicted (Bii). Electron micrographs were obtained from 3 mo YAC128 and WT mice striatum and mitochondrial morphology presented for area, perimeter, aspect ratio and circularity as evaluated by Fiji-imageJ software (C). Over 62 individual mitochondria were assessed in independent preparations from 6 independent TEM images from WT and YAC128 mice (scale bar: 1000 nm). Data are the mean \pm SEM of experiments performed in independent mitochondrial preparations obtained from 3 to 16 mice from each genotype run in triplicates to quadruplicates. In (A) results are presented in relation to the unit (dashed line) representing the WT mouse values. Statistical analysis: * $p < 0.05$, ** $p < 0.01$, **** $p < 0.0001$ when compared with WT mitochondria, by nonparametric Mann-Whitney U test. (For interpretation of the references to color in this figure legend, the reader is referred to the Web version of this article.)

amyotrophic lateral sclerosis patients, as evaluated by PET using [^{62}Cu]-ATSM and further associated with disease severity in both diseases [24,25,50].

In Huntington's disease, mHTT is widely expressed in all body cells which highlights the importance of energy metabolism studies in peripheral cells. A previous study stressed that fibroblasts from healthy donors and Huntington's disease patients exhibited different profiles if stratified according to motor function, psychiatric and functional capacity. Fibroblasts obtained from manifest Huntington's disease patients displayed compromised cell growth and reduced ATP production, accompanied by decreased mitochondrial activity, which was indicative of respiratory chain defects [15]. Of interest, the age at onset seems to be a crucial element together with CAG expansion to define the bioenergetic profile of fibroblasts of Huntington's disease patients [14].

Similarly, our data suggests that Huntington's disease patients symptomatic for longer periods of time have highly compromised mitochondrial function. In these cells, a slight increase in mitochondrial ROS was reported, despite a significant elevation in antioxidant enzymes (SOD2 and GR) [15], while other authors described a decrease in catalase activity in Huntington's disease fibroblasts [22]. Impaired antioxidant defenses, namely a decrease in GPx and SOD1 activities, were also observed in erythrocytes from Huntington's disease patients [51]. Previous studies performed in our lab showed increased mitochondrial-driven ROS in Huntington's disease human cybrids [18]

and mouse striatal cells expressing full-length mHTT [20,21,52,53]. An increase in ROS was also found in the brain striatum and cortex of symptomatic R6/1 [54], R6/2 mouse models [55,56] and in YAC128 embryonic fibroblasts and fibroblasts derived from Huntington's disease patients [57]. In YAC128 mouse striatal and cortical brain mitochondria enhanced levels of H_2O_2 did not account for by changes in antioxidant profile.

Mitochondrial function has a significant impact on organelle morphology, defined by a regulated balance between fission and fusion events. Loss of bioenergetic capacity results in an inability to maintain the mitochondrial network organization [58]. In our study, skin fibroblast mitochondria from Pre-M Huntington's disease carriers became larger, whereas circularity decreased, when compared to healthy controls and manifest patients. These ultrastructural characteristics suggest a promotion of mitochondrial fusion events that might be required to maximize oxidative phosphorylation. Conversely, striatal mitochondria from pre-symptomatic YAC128 mice, retaining mHTT interaction, exhibited increased circularity, as revealed by ultrastructure analysis. These results might be determined by striatal mitochondria-specific vulnerability in Huntington's disease. Accordingly, fragmented mitochondria were previously reported in many Huntington's disease cell models, including peripheral cells (e.g. Ref. [59]). Mitochondrial fragmentation was previously observed in rat cortical neurons expressing mHTT and in fibroblasts from manifest Huntington's disease patients

and in YAC128 Huntington's disease mouse model, before the appearance of neurological deficits and mHTT aggregates [60]; in striatum of YAC128 mice, an increase in the number of small mitochondria and decreased cristae surface area were also detected [60].

Decreased ability to take up Ca^{2+} through the MCU was further observed in striatal mitochondrial-enriched fractions from pre-symptomatic YAC128 mice, when compared to cortical mitochondria, again underlying a highly dysfunctional organelle derived from the striatum. Defects on mitochondrial Ca^{2+} handling were previously demonstrated in lymphoblast mitochondria from Huntington's disease patients and brain mitochondria from YAC128 mice [61], isolated mitochondria from transgenic Huntington's disease rats with 51 CAG repeats [62] and in mutant mouse striatal cell line [63,64]. Concordantly, in striatal mitochondria obtained from rat brain, lower calcium levels consistently evoked a permeability transition more easily than in cortical mitochondria [65]. Conversely, an increase in Ca^{2+} loading capacity in forebrain (brain minus the cerebellum)-derived mitochondria from R6/2 and YAC128 mice, but not in organelle isolated from Hdh150 knock-in mice, was observed [16]. More recently, a large Ca^{2+} uptake capacity in synaptic and nonsynaptic mitochondria isolated from 2 to 12 mo YAC128 mice brain, when compared with YAC18 or FVB/NJ mice [35] was reported. Indeed, changes in mitochondrial Ca^{2+} handling have not been consistent in Huntington's disease models, particularly when studying isolated brain mitochondria, which might be related with different methodologies of isolating the organelle and/or assessing ion changes, as well as the isolated brain tissue.

The number of mtDNA copies has a crucial role in cellular metabolism and bioenergetics. The mechanisms responsible for regulation of mtDNA copy number in Huntington's disease pathology are still under discussion. Our study reveals that Pre-M Huntington's disease carriers harbor a higher number of mtDNA copies; interestingly, a strong and significant correlation was observed with enhanced mitochondrial bioenergetics and [^{64}Cu]-ATSM uptake. Contradictory conclusions may be dependent on the cell type, as shown by a significantly higher mtDNA/nDNA copy number in leukocytes, but lower in fibroblasts from manifest Huntington's disease patients [66]. Moreover, mtDNA copy number was increased before disease onset in leukocytes of Huntington's disease mutation carriers and declined after disease onset [67].

Of relevance, this study provides novel and important data suggesting a compensatory mechanism in premanifest and prodromal Huntington's disease carriers and pre-symptomatic Huntington's disease mice model to overcome the early insults, particularly the underlying oxidative stress. Compensatory mechanisms at early stages of age-related brain diseases, as determined in human and mouse, have been described elsewhere [68,69]. Reports of upregulation in the expression of mitochondrial-encoded genes in blood samples of mild cognitively impaired patients, compared to Alzheimer's disease patients and healthy controls, suggested a compensatory-like mechanism at the early stages of disease [70,71].

Overall, this study provides novel data regarding *in vivo* PET analysis showing accumulation of [^{64}Cu]-ATSM that correlates with major redox changes and mitochondrial deregulation at very early stages in Huntington's disease. Increased oxygen consumption rates concomitantly with enhanced ROS levels at early/presymptomatic Huntington's disease stages (as observed in both human and mouse mHTT carriers) reinforce the hypothesis that mitochondrial and redox deregulation contribute to Huntington's disease pathogenesis. Thus, apparently compensatory mitochondrial changes occurring in Huntington's disease presymptomatic stages might constitute a biomarker of therapeutic response, as previously tested by us in pridopidine-treated YAC128 mice [12].

The major limitation of the current study is the small number of participants. Further studies with a larger number of participants and at different disease stages are necessary to validate the human data. Nonetheless, the overlapping results obtained in mitochondrial function and oxidative stress in pre-symptomatic stages in YAC128 mice supports

the changes reported in Huntington's disease carriers. Moreover, data in mouse striatum reinforces an increased susceptibility of this brain region in Huntington's disease. Thus, potential benefits of early therapeutic interventions based on mitochondrial-targeted compounds aiming to regularize mitochondrial function and reduce ROS generation, particularly in the striatum, are anticipated to help to slowdown Huntington's disease progression.

Funding

This work was financed by Mantero Belard Neuroscience prize 2013 (1st Edition), supported by Santa Casa da Misericórdia de Lisboa (SCML), Portugal; 'FLAD Life Science 2020' prize, funded by 'Fundação Luso-Americana para o Desenvolvimento' (FLAD), Portugal; European Regional Development Fund (ERDF), through the Centro 2020 Regional Operational Programme under project CENTRO-01-0145-FEDER-000012-HealthyAging2020 and through COMPETE 2020 - Operational Programme for Competitiveness and Internationalisation and Portuguese national funds via FCT – *Fundação para a Ciência e a Tecnologia*, under projects UIDB/04539/2020, UIDP/04539/2020 and LA/P/0058/2020.

Ferreira IL was supported by Mantero Belard Neuroscience prize 2013 (1st Edition), SCML post-doctoral fellowship and FCT postdoctoral fellowship SFRH/BPD/108493/2015; Mota SI and Laço M were supported by FCT postdoctoral fellowships SFRH/BPD/99219/2013 and SFRH/BPD/91811/2012, respectively.

Project operational support for Michael R. Hayden provided by a Canadian Institutes of Health Research (CIHR) Foundation grant (FDN 154278). Michael R. Hayden is a Canada Research Chair in Human Genetics and Molecular Medicine.

Declaration of competing interest

The authors report no competing interests.

Data availability

Data will be made available on request.

Acknowledgements

We acknowledge Dr. Mónica Zuzarte, for fibroblasts and mouse brain TEM analyses at the 'Laboratório de Bio-imagem de Alta Resolução' of the Faculty of Medicine of the University of Coimbra.

Appendix A. Supplementary data

Supplementary data to this article can be found online at <https://doi.org/10.1016/j.redox.2022.102424>.

References

- [1] THSDCR. Group, A novel gene containing a trinucleotide repeat that is expanded and unstable on Huntington's disease chromosomes. The Huntington's Disease Collaborative Research Group, *Cell*. 72 (6) (Mar 26 1993) 971–983, [https://doi.org/10.1016/0092-8674\(93\)90585-e](https://doi.org/10.1016/0092-8674(93)90585-e).
- [2] M. Damiano, L. Galvan, N. Deglon, E. Brouillet, Mitochondria in Huntington's disease, *Biochimica et biophysica acta*. Jan 1802 (1) (2010) 52–61, <https://doi.org/10.1016/j.bbdis.2009.07.012>.
- [3] V. Costa, L. Scorrano, Shaping the role of mitochondria in the pathogenesis of Huntington's disease, *EMBO J*. 31 (8) (Apr 18 2012) 1853–1864, <https://doi.org/10.1038/emboj.2012.65>.
- [4] L. Naia, I.L. Ferreira, E. Ferreira, A.C. Rego, Mitochondrial Ca^{2+} handling in Huntington's and Alzheimer's diseases - role of ER-mitochondria crosstalk, *Biochem. Biophys. Res. Commun.* 483 (4) (Feb 19 2017) 1069–1077, <https://doi.org/10.1016/j.bbrc.2016.07.122>.
- [5] W.A. Brennan, E.D. Bird, J.R. Aprille, Regional mitochondrial respiratory activity in Huntington's disease brain, *J Neurochem.* 44 (6) (Jun 1985) 1948–1950, <https://doi.org/10.1111/j.1471-4159.1985.tb07192.x>.

- [6] S.E. Browne, A.C. Bowling, U. MacGarvey, et al., Oxidative damage and metabolic dysfunction in Huntington's disease: selective vulnerability of the basal ganglia, *Ann Neurol* 41 (5) (May 1997) 646–653, <https://doi.org/10.1002/ana.410410514>.
- [7] M. Gu, M.T. Gash, V.M. Mann, F. Javoy-Agid, J.M. Cooper, A.H. Schapira, Mitochondrial defect in Huntington's disease caudate nucleus, *Ann Neurol* 39 (3) (Mar 1996) 385–389, <https://doi.org/10.1002/ana.410390317>.
- [8] M. Damiano, E. Diguett, C. Malgorn, et al., A role of mitochondrial complex II defects in genetic models of Huntington's disease expressing N-terminal fragments of mutant huntingtin, *Hum. Mol. Genet.* 22 (19) (Oct 1 2013) 3869–3882, <https://doi.org/10.1093/hmg/ddt242>.
- [9] J. Hamilton, J.J. Pellman, T. Brustovetsky, R.A. Harris, N. Brustovetsky, Oxidative metabolism in YAC128 mouse model of Huntington's disease, *Hum. Mol. Genet.* 24 (17) (Sep 1 2015) 4862–4878, <https://doi.org/10.1093/hmg/ddv209>.
- [10] J. Hamilton, T. Brustovetsky, N. Brustovetsky, Oxidative metabolism and Ca²⁺ handling in striatal mitochondria from YAC128 mice, a model of Huntington's disease, *Neurochem. Int.* 109 (Oct 2017) 24–33, <https://doi.org/10.1016/j.neuint.2017.01.001>.
- [11] J. Hamilton, J.J. Pellman, T. Brustovetsky, R.A. Harris, N. Brustovetsky, Oxidative metabolism and Ca²⁺ handling in isolated brain mitochondria and striatal neurons from R6/2 mice, a model of Huntington's disease, *Hum. Mol. Genet.* 25 (13) (Jul 1 2016) 2762–2775, <https://doi.org/10.1093/hmg/ddw133>.
- [12] L. Naia, P. Ly, S.I. Mota, et al., The sigma-1 receptor mediates pridopidine rescue of mitochondrial function in Huntington disease models, *Neurotherapeutics* (Apr 2021), <https://doi.org/10.1007/s13311-021-01022-9>.
- [13] A.C. Silva, S. Almeida, M. Laço, et al., Mitochondrial respiratory chain complex activity and bioenergetic alterations in human platelets derived from pre-symptomatic and symptomatic Huntington's disease carriers, *Mitochondrion* 13 (6) (Nov 2013) 801–809, <https://doi.org/10.1016/j.mito.2013.05.006>.
- [14] S.L. Gardiner, C. Milanese, M.W. Boogaard, et al., Bioenergetics in fibroblasts of patients with Huntington disease are associated with age at onset, *Neuro Genet* 4 (5) (Oct 2018) e275, <https://doi.org/10.1212/NXG.0000000000000275>.
- [15] P. Jedrak, P. Mozolewski, G. Wegryz, M.R. Więckowski, Mitochondrial alterations accompanied by oxidative stress conditions in skin fibroblasts of Huntington's disease patients, *Metab. Brain Dis.* 33 (6) (2018) 2005–2017, <https://doi.org/10.1007/s11011-018-0308-1>.
- [16] J.M. Oliveira, M.B. Jekabsons, S. Chen, et al., Mitochondrial dysfunction in Huntington's disease: the bioenergetics of isolated and in situ mitochondria from transgenic mice, *J. Neurochem.* 101 (1) (Apr 2007) 241–249, <https://doi.org/10.1111/j.1471-4159.2006.04361.x>.
- [17] J.M. Oliveira, S. Chen, S. Almeida, et al., Mitochondrial-dependent Ca²⁺ handling in Huntington's disease striatal cells: effect of histone deacetylase inhibitors, *J. Neurosci.* 26 (43) (Oct 2006) 11174–11186, <https://doi.org/10.1523/JNEUROSCI.3004-06.2006>.
- [18] L.L. Ferreira, M.V. Nascimento, M. Ribeiro, et al., Mitochondrial-dependent apoptosis in Huntington's disease human cybrids, *Experimental neurology* 222 (2) (Apr 2010) 243–255, <https://doi.org/10.1016/j.expneurol.2010.01.002>.
- [19] L.L. Ferreira, T. Cunha-Oliveira, M.V. Nascimento, et al., Bioenergetic dysfunction in Huntington's disease human cybrids, *Experimental neurology* 231 (1) (Sep 2011) 127–134, <https://doi.org/10.1016/j.expneurol.2011.05.024>.
- [20] M. Ribeiro, T.R. Rosenstock, T. Cunha-Oliveira, L.L. Ferreira, C.R. Oliveira, A. C. Rego, Glutathione redox cycle dysregulation in Huntington's disease knock-in striatal cells, *Free radical biology & medicine* 53 (10) (Nov 15 2012) 1857–1867, <https://doi.org/10.1016/j.freeradbiomed.2012.09.004>.
- [21] M. Ribeiro, T.R. Rosenstock, A.M. Oliveira, C.R. Oliveira, A.C. Rego, Insulin and IGF-1 improve mitochondrial function in a PI-3K/Akt-dependent manner and reduce mitochondrial generation of reactive oxygen species in Huntington's disease knock-in striatal cells, *Free radical biology & medicine* 74 (Sep 2014) 129–144, <https://doi.org/10.1016/j.freeradbiomed.2014.06.023>.
- [22] P. del Hoyo, A. García-Redondo, F. de Bustos, et al., Oxidative stress in skin fibroblasts cultures of patients with Huntington's disease, *Neurochem Res.* Sep 31 (9) (2006) 1103–1109, <https://doi.org/10.1007/s11064-006-9110-2>.
- [23] A. Sawa, G.W. Wiegand, J. Cooper, et al., Increased apoptosis of Huntington disease lymphoblasts associated with repeat length-dependent mitochondrial depolarization, *Nat Med.* 5 (10) (Oct 1999) 1194–1198, <https://doi.org/10.1038/13518>.
- [24] M. Ikawa, H. Okazawa, T. Kudo, M. Kuriyama, Y. Fujibayashi, M. Yoneda, Evaluation of striatal oxidative stress in patients with Parkinson's disease using [62Cu]ATSM PET, *Nucl Med Biol* 38 (7) (Oct 2011) 945–951, <https://doi.org/10.1016/j.nucmedbio.2011.02.016>.
- [25] M. Ikawa, H. Okazawa, T. Tsujikawa, et al., Increased oxidative stress is related to disease severity in the ALS motor cortex: a PET study, *Neurology* 84 (20) (May 2015) 2033–2039, <https://doi.org/10.1212/WNL.0000000000000588>.
- [26] M. Ikawa, H. Okazawa, K. Arakawa, et al., PET imaging of redox and energy states in stroke-like episodes of MELAS, *Mitochondrion.* Apr 9 (2) (2009) 144–148, <https://doi.org/10.1016/j.mito.2009.01.011>.
- [27] Y. Yoshii, M. Yoneda, M. Ikawa, et al., Radiolabeled Cu-ATSM as a novel indicator of overreduced intracellular state due to mitochondrial dysfunction: studies with mitochondrial DNA-less p0 cells and cybrids carrying MELAS mitochondrial DNA mutation, *Nucl Med Biol* 39 (2) (Feb 2012) 177–185, <https://doi.org/10.1016/j.nucmedbio.2011.08.008>.
- [28] R. Reilmann, B.R. Leavitt, C.A. Ross, Diagnostic criteria for Huntington's disease based on natural history, *Mov. Disord.* 29 (11) (Sep 15 2014) 1335–1341, <https://doi.org/10.1002/mds.26011>.
- [29] M. Matarrese, P. Bedeschi, R. Scardaoni, et al., Automated production of copper radioisotopes and preparation of high specific activity [(64)Cu]Cu-ATSM for PET studies, *Applied radiation and isotopes* : including data, instrumentation and methods for use in agriculture, industry and medicine 68 (1) (Jan 2010) 5–13, <https://doi.org/10.1016/j.apradiso.2009.08.010>.
- [30] M.A. Pouladi, Y. Xie, N.H. Skotte, et al., Full-length huntingtin levels modulate body weight by influencing insulin-like growth factor 1 expression, *Hum. Mol. Genet.* 19 (8) (Apr 15 2010) 1528–1538, <https://doi.org/10.1093/hmg/ddq026>.
- [31] C. Lopes, M. Ribeiro, A.I. Duarte, et al., IGF-1 intranasal administration rescues Huntington's disease phenotypes in YAC128 mice, *Molecular neurobiology.* Jun 49 (3) (2014) 1126–1142, <https://doi.org/10.1007/s12035-013-8585-5>.
- [32] P. Martins, A. Blanco, P. Crespo, et al., Towards very high resolution RPC-PET for small animals, *J. Instrum.* 9 (2014), C10012, <https://doi.org/10.1088/1748-0221/9/10/C10012>.
- [33] I. Onofre, N. Mendonça, S. Lopes, et al., Fibroblasts of Machado Joseph Disease patients reveal autophagy impairment, *Sci Rep.* 6 (06 2016), 28220, <https://doi.org/10.1038/srep28220>.
- [34] L.L. Ferreira, C. Carmo, L. Naia, S. I Mota, A. Cristina Rego, Assessing mitochondrial function in vitro and ex vivo models of Huntington's disease, *Methods Mol. Biol.* 1780 (2018) 415–442, https://doi.org/10.1007/978-1-4939-7825-0_19.
- [35] J.J. Pellman, J. Hamilton, T. Brustovetsky, N. Brustovetsky, Ca²⁺ handling in isolated brain mitochondria and cultured neurons derived from the YAC128 mouse model of Huntington's disease, *J Neurochem.* 134 (4) (Aug 2015) 652–667, <https://doi.org/10.1111/jnc.13165>.
- [36] Group. THS., Unified Huntington's disease rating scale: reliability and consistency, *Mov Disord.* 11 (2) (Mar 1996) 136–142, <https://doi.org/10.1002/mds.870110204>.
- [37] T. Liu, M. Karlsen, A.M. Karlberg, K.R. Redalen, Hypoxia imaging and theranostic potential of, *EJNMMI Res.* Apr 09 10 (1) (2020) 33, <https://doi.org/10.1186/s13550-020-00621-5>.
- [38] N.Z. Hobbs, J. Barnes, C. Frost, et al., Onset and progression of pathologic atrophy in Huntington disease: a longitudinal MR imaging study, *AJNR Am J Neuroradiol.* 31 (6) (Jun 2010) 1036–1041, <https://doi.org/10.3174/ajnr.A2018>.
- [39] D.L. Harrington, J.D. Long, S. Durgierian, et al., Cross-sectional and longitudinal multimodal structural imaging in prodromal Huntington's disease, *Mov. Disord.* 31 (11) (2016) 1664–1675, <https://doi.org/10.1002/mds.26803>.
- [40] M.J. Novak, K.K. Seunarine, C.R. Gibbard, et al., White matter integrity in premanifest and early Huntington's disease is related to caudate loss and disease progression, *Cortex.* 52 (Mar 2014) 98–112, <https://doi.org/10.1016/j.cortex.2013.11.009>.
- [41] M. Colombié, S. Gouard, M. Frindel, et al., Focus on the controversial aspects of (64)Cu-ATSM in tumoral hypoxia mapping by PET imaging, *Front. Med.* 2 (2015) 58, <https://doi.org/10.3389/fmed.2015.00058>.
- [42] J.F. Atherton, E.L. McIver, M.R. Mullen, D.L. Wokosin, D.J. Surmeier, M.D. Bevan, Early dysfunction and progressive degeneration of the subthalamic nucleus in mouse models of Huntington's disease, *Elife* 12 (2016) 5, <https://doi.org/10.7554/eLife.21616>.
- [43] J.W. Callahan, E.D. Abercrombie, Relationship between subthalamic nucleus neuronal activity and electrocorticogram is altered in the R6/2 mouse model of Huntington's disease, *J Physiol.* 593 (16) (Aug 2015) 3727–3738, <https://doi.org/10.1113/JP270268>.
- [44] M.S. Goyal, A.G. Vlassenko, T.M. Blazey, et al., Loss of brain aerobic glycolysis in normal human aging, *Cell Metabol.* 26 (2) (Aug 01 2017) 353–360, <https://doi.org/10.1016/j.cmet.2017.07.010>.
- [45] A. Bratic, N.G. Larsson, The role of mitochondria in aging, *J Clin Invest.* 123 (3) (Mar 2013) 951–957, <https://doi.org/10.1172/JCI64125>.
- [46] M.H. Petersen, C.W. Willert, J.V. Andersen, et al., Progressive mitochondrial dysfunction of striatal synapses in R6/2 mouse model of Huntington's disease, *J Huntingtons Dis* 11 (2) (2022) 121–140, <https://doi.org/10.3233/JHD-210518>.
- [47] A.M. Pickrell, H. Fukui, X. Wang, M. Pinto, C.T. Moraes, The striatum is highly susceptible to mitochondrial oxidative phosphorylation dysfunctions, *J. Neurosci.* : the official journal of the Society for Neuroscience 31 (27) (Jul 6 2011) 9895–9904, <https://doi.org/10.1523/JNEUROSCI.6223-10.2011>.
- [48] L.I. Petrella, J.M. Castelhan, M. Ribeiro, et al., A whole brain longitudinal study in the YAC128 mouse model of Huntington's disease shows distinct trajectories of neurochemical, structural connectivity and volumetric changes, *Hum. Mol. Genet.* 27 (12) (Jun 15 2018) 2125–2137, <https://doi.org/10.1093/hmg/ddy119>.
- [49] P.S. Donnelly, J.R. Liddell, S. Lim, et al., An impaired mitochondrial electron transport chain increases retention of the hypoxia imaging agent diacetyl-bis(4-methylthiosemicarbazone)copper(II), *Proc Natl Acad Sci U S A* 109 (1) (Jan 2012) 47–52, <https://doi.org/10.1073/pnas.1116227108>.
- [50] H. Neishi, M. Ikawa, H. Okazawa, et al., Precise evaluation of striatal oxidative stress corrected for severity of dopaminergic neuronal degeneration in patients with Parkinson's disease: a study with 62Cu-ATSM PET and 123I-FP-CIT SPECT, *Eur. Neurol.* 78 (3–4) (2017) 161–168, <https://doi.org/10.1159/000479627>.
- [51] C.M. Chen, Y.R. Wu, M.L. Cheng, et al., Increased oxidative damage and mitochondrial abnormalities in the peripheral blood of Huntington's disease patients, *Biochem. Biophys. Res. Commun.* 359 (2) (Jul 27 2007) 335–340, <https://doi.org/10.1016/j.bbrc.2007.05.093>.
- [52] M. Ribeiro, A.C. Silva, J. Rodrigues, L. Naia, A.C. Rego, Oxidizing effects of exogenous stressors in Huntington's disease knock-in striatal cells—protective effect of cystamine and creatine, *Toxicol. Sci.* : an official journal of the Society of Toxicology 136 (2) (Dec 2013) 487–499, <https://doi.org/10.1093/toxsci/kft199>.
- [53] A.M. Oliveira, S.M. Cardoso, M. Ribeiro, R.S. Seixas, A.M. Silva, A.C. Rego, Protective effects of 3-alkyl luteolin derivatives are mediated by Nrf 2 transcriptional activity and decreased oxidative stress in Huntington's disease mouse striatal cells, *Neurochem. Int.* 91 (Dec 2015) 1–12, <https://doi.org/10.1016/j.neuint.2015.10.004>.

- [54] F. Perez-Severiano, A. Santamaria, J. Pedraza-Chaverri, O.N. Medina-Campos, C. Rios, J. Segovia, Increased formation of reactive oxygen species, but no changes in glutathione peroxidase activity, in striata of mice transgenic for the Huntington's disease mutation, *Neurochem. Res.* 29 (4) (Apr 2004) 729–733, <https://doi.org/10.1023/b:nere.0000018843.83770.4b>.
- [55] M. Sadagurski, Z. Cheng, A. Rozzo, et al., IRS2 increases mitochondrial dysfunction and oxidative stress in a mouse model of Huntington disease, *J. Clin. Invest.* 121 (10) (Oct 2011) 4070–4081, <https://doi.org/10.1172/JCI46305>.
- [56] S.J. Tabrizi, J. Workman, P.E. Hart, et al., Mitochondrial dysfunction and free radical damage in the Huntington R6/2 transgenic mouse, *Annals of neurology* 47 (1) (Jan 2000) 80–86, [https://doi.org/10.1002/1531-8249\(200001\)47:1<80::aid-ana13>3.3.co;2-b](https://doi.org/10.1002/1531-8249(200001)47:1<80::aid-ana13>3.3.co;2-b).
- [57] J.Q. Wang, Q. Chen, X. Wang, et al., Dysregulation of mitochondrial calcium signaling and superoxide flashes cause mitochondrial genomic DNA damage in Huntington disease, *J. Biol. Chem.* 288 (5) (Feb 1 2013) 3070–3084, <https://doi.org/10.1074/jbc.M112.407726>.
- [58] C. Lopes, Y. Tang, S.I. Anjo, B. Manadas, I. Onofre, L.P. De Almeida, G.Q. Daley, T. M. Schlaeger, A.C. Rego, Mitochondrial and redox modifications in Huntington disease induced pluripotent stem cells rescued by CRISPR/Cas9 CAGs targeting, *Front. Cell Dev. Biol.* 8 (2020), <https://doi.org/10.3389/fcell.2020.576592>.
- [59] M.J. Mihm, D.M. Amann, B.L. Schanbacher, R.A. Altschuld, J.A. Bauer, K.R. Hoyt, Cardiac dysfunction in the R6/2 mouse model of Huntington's disease, *Neurobiology of disease* 25 (2) (Feb 2007) 297–308, <https://doi.org/10.1016/j.nbd.2006.09.016>.
- [60] W. Song, J. Chen, A. Petrilli, et al., Mutant huntingtin binds the mitochondrial fission GTPase dynamin-related protein-1 and increases its enzymatic activity. *Nature medicine*, Mar 17 (3) (2011) 377–382, <https://doi.org/10.1038/nm.2313>.
- [61] A.V. Panov, C.A. Gutekunst, B.R. Leavitt, et al., Early mitochondrial calcium defects in Huntington's disease are a direct effect of polyglutamines, *Nature neuroscience* 5 (8) (Aug 2002) 731–736, <https://doi.org/10.1038/nn884>.
- [62] F.N. Gellerich, Z. Gizatullina, H.P. Nguyen, et al., Impaired regulation of brain mitochondria by extramitochondrial Ca²⁺ in transgenic Huntington disease rats, *J. Biol. Chem.* 283 (45) (Nov 7 2008) 30715–30724, <https://doi.org/10.1074/jbc.M709555200>.
- [63] D. Lim, L. Fedrizzi, M. Tartari, et al., Calcium homeostasis and mitochondrial dysfunction in striatal neurons of Huntington disease, *J. Biol. Chem.* 283 (9) (Feb 29 2008) 5780–5789, <https://doi.org/10.1074/jbc.M704704200>.
- [64] T. Milakovic, R.A. Quintanilla, G.V. Johnson, Mutant huntingtin expression induces mitochondrial calcium handling defects in clonal striatal cells: functional consequences, *J. Biol. Chem.* 281 (46) (Nov 17 2006) 34785–34795, <https://doi.org/10.1074/jbc.M603845200>.
- [65] N. Brustovetsky, T. Brustovetsky, K.J. Purl, M. Capano, M. Crompton, J. M. Dubinsky, Increased susceptibility of striatal mitochondria to calcium-induced permeability transition, *J Neurosci* 23 (12) (Jun 15 2003) 4858–4867.
- [66] P. Jędrak, M. Krygier, K. Tońska, et al., Mitochondrial DNA levels in Huntington disease leukocytes and dermal fibroblasts, *Metab Brain Dis.* 32 (4) (08 2017) 1237–1247, <https://doi.org/10.1007/s11011-017-0026-0>.
- [67] M.H. Petersen, E. Budtz-Jørgensen, S.A. Sørensen, et al., Reduction in mitochondrial DNA copy number in peripheral leukocytes after onset of Huntington's disease, *Mitochondrion* 17 (Jul 2014) 14–21, <https://doi.org/10.1016/j.mito.2014.05.001>.
- [68] A. Ashraf, Z. Fan, D.J. Brooks, P. Edison, Cortical hypermetabolism in MCI subjects: a compensatory mechanism? *Eur J Nucl Med Mol Imaging* 42 (3) (Mar 2015) 447–458, <https://doi.org/10.1007/s00259-014-2919-z>.
- [69] G. Rudow, R. O'Brien, A.V. Savonenko, et al., Morphometry of the human substantia nigra in ageing and Parkinson's disease, *Acta Neuropathol.* 115 (4) (Apr 2008) 461–470, <https://doi.org/10.1007/s00401-008-0352-8>.
- [70] K. Lunnon, A. Keohane, R. Pidsley, et al., Mitochondrial genes are altered in blood early in Alzheimer's disease, *Neurobiol Aging* 53 (05 2017) 36–47, <https://doi.org/10.1016/j.neurobiolaging.2016.12.029>.
- [71] D. Mastroeni, O.M. Khdour, E. Delvaux, et al., Nuclear but not mitochondrial-encoded oxidative phosphorylation genes are altered in aging, mild cognitive impairment, and Alzheimer's disease, *Alzheimers Dement.* 13 (5) (May 2017) 510–519, <https://doi.org/10.1016/j.jalz.2016.09.003>.